

Dynamical Mass of the Substellar Benchmark Binary HD 130948BC^{1,2,3}Trent J. Dupuy,⁴ Michael C. Liu,^{4,5} Michael J. Ireland⁶**ABSTRACT**

We present Keck adaptive optics imaging of the L4+L4 binary HD 130948BC along with archival *HST* and Gemini-North observations, which together span $\approx 70\%$ of the binary's orbital period. From the relative orbit, we determine a total dynamical mass of $0.109 \pm 0.002 M_{\odot}$ ($114 \pm 2 M_{\text{Jup}}$). The flux ratio of HD 130948BC is near unity, so both components are unambiguously substellar for any plausible mass ratio. An independent constraint on the age of the system is available from the primary HD 130948A (G2V, $[M/H] = 0.0$). The ensemble of available indicators suggests an age comparable to the Hyades, with the most precise age being $0.79^{+0.22}_{-0.15}$ Gyr based on gyrochronology. Therefore, HD 130948BC is now a unique benchmark among field L and T dwarfs, with a well-determined mass, luminosity, and age. We find that substellar theoretical models disagree with our observations. (1) Both components of HD 130948BC appear to be overluminous by a factor of $\approx 2\text{--}3\times$ compared to evolutionary models. The age of the system would have to be notably younger than the gyro age to ameliorate the luminosity disagreement. (2) Effective temperatures derived from evolutionary models for HD 130948B and C are inconsistent with temperatures determined from spectral synthesis for objects of similar spectral type. Overall, regardless of the adopted age, evolutionary and atmospheric models give inconsistent results, which indicates systematic

¹Most of the data presented herein were obtained at the W.M. Keck Observatory, which is operated as a scientific partnership among the California Institute of Technology, the University of California, and the National Aeronautics and Space Administration. The Observatory was made possible by the generous financial support of the W.M. Keck Foundation.

²Based on observations made with the NASA/ESA *Hubble Space Telescope*, obtained from the data archive at the Space Telescope Institute. STScI is operated by the association of Universities for Research in Astronomy, Inc. under the NASA contract NAS 5-26555.

³Based on observations obtained at the Gemini Observatory, which is operated by the Association of Universities for Research in Astronomy, Inc., under a cooperative agreement with the NSF on behalf of the Gemini partnership: the National Science Foundation (United States), the Science and Technology Facilities Council (United Kingdom), the National Research Council (Canada), CONICYT (Chile), the Australian Research Council (Australia), Ministério da Ciência e Tecnologia (Brazil) and SECYT (Argentina).

⁴Institute for Astronomy, University of Hawai'i, 2680 Woodlawn Drive, Honolulu, HI 96822; tdupuy@ifa.hawaii.edu

⁵Alfred P. Sloan Research Fellow

⁶School of Physics, University of Sydney, NSW 2006, Australia

errors in at least one class of models, possibly both. The masses of HD 130948BC happen to be very near the theoretical mass limit for lithium burning, and thus measuring the differential lithium depletion between B and C will provide a uniquely discriminating test of theoretical models. The potential underestimate of luminosities by evolutionary models would have wide-ranging implications; therefore, a more refined age estimate for HD 130948A is critically needed.

Subject headings: binaries: general, close — stars: brown dwarfs — infrared: stars — techniques: high angular resolution

1. Introduction

More than a decade after their discovery, brown dwarfs continue to offer key insights into the astrophysics governing of some of the lowest temperature products of star formation. Brown dwarfs in the field are particularly useful as probes of very cold atmospheres. For instance, the atmospheres of extrasolar planets are very difficult to study directly due to their intrinsic faintness and proximity to very bright stars. However, brown dwarfs are typically found in relative isolation, and their atmospheres are subject to the same processes (e.g., dust formation and sedimentation, and non-equilibrium molecular chemistry) that are at work in their much less massive planetary counterparts.

Despite the broad relevance of brown dwarfs, their fundamental properties remain poorly constrained by observations. In particular, very few direct mass measurements are available for brown dwarfs. To date, a total of six objects have been identified as unambiguously substellar ($M < 0.072 M_{\odot}$ at solar metallicity; Chabrier & Baraffe 2000) via dynamical mass measurements with precisions ranging from 6–9%: both components of the T5.0+T5.5 binary 2MASS J15344984–2952274AB (Liu et al. 2008), both components of the young M6.5+M6.5 eclipsing binary 2MASS J05352184–0546085 in the Orion Nebula (Stassun et al. 2006), and two tertiary components of hierarchical triples in which the primaries are M stars, GJ 802B (Ireland et al. 2008) and Gl 569Bb (Lane et al. 2001; Zapatero Osorio et al. 2004; Simon et al. 2006). Direct mass measurements of brown dwarfs are critical for empirically constraining substellar evolutionary models. Since brown dwarfs have no sustainable source of internal energy, they follow a mass–luminosity–age relation, rather than the simpler mass–luminosity relation for main-sequence stars. Thus, mass measurements alone cannot fully constrain theoretical models, although mass and luminosity measurements of brown dwarfs in coeval binary systems can offer stringent tests of theoretical models (e.g., Liu et al. 2008). To fully constrain evolutionary models, systems with independent measurements of the mass, age, and L_{bol} (or one of the much less observationally accessible quantities T_{eff} or R) are required. Such systems are quite rare, but they represent the gold standard among “benchmark” brown dwarfs.

Potter et al. (2002) discovered the L dwarf binary HD 130948BC in a hierarchical triple configuration with the young solar analog HD 130948A (G2V) using the curvature adaptive optics

(AO) system Hokupa‘a on the Gemini North Telescope on 2001 February 24 UT. The L dwarfs are separated from each other by $\lesssim 0''.13$, and they lie $2''.6$ from the primary G star. HD 130948BC has been the target of AO-fed slit spectroscopy with NIRSPEC on the Keck II Telescope (1.15–1.35 μm) and IRCS on the Subaru Telescope (1.5–1.8 μm , 1.95–2.4 μm). Goto et al. (2002) used the latter spectra to determine the spectral types of the B and C components, both $L4\pm 1$, via spectral template matching. These are consistent with the less precise NIRSPEC J -band spectral types of $dL2\pm 2$, which are on the Martín et al. (1999) system, found by Potter et al. (2002) for both HD 130948B and C.

We present here a dynamical mass measurement for HD 130948BC based on Keck natural guide star adaptive optics (NGS AO) imaging of HD 130948BC, as well as an analysis of *Hubble Space Telescope* (*HST*) and Gemini archival images. In addition to an independent age estimate ($0.79_{-0.15}^{+0.22}$ Gyr, see §4), the primary star provides a wealth of information about the system. Valenti & Fischer (2005) measured a solar metallicity for HD 130948A ($[M/H] = 0.00$, $[Fe/H] = 0.05$), which is important since metallicity can play a significant role in shaping the spectra of brown dwarfs (e.g., Burrows et al. 2006; Liu et al. 2007). Most importantly, the distance to HD 130948A has been measured very precisely by *Hipparcos*, with a revised parallax of 55.01 ± 0.24 mas (van Leeuwen 2007), corresponding to a distance of $d = 18.18\pm 0.08$ pc. Thus, the distance is measured to an exquisite precision of 0.44%, which is invaluable since the error in the dynamical mass scales as $3\times$ the distance error (i.e., the 0.44% error in distance translates into a 1.3% error in mass).

HD 130948BC can thus serve as both an “age benchmark” and “mass benchmark” system in studying brown dwarfs. In the literature, the term benchmark is often applied to any readily observable unique or extreme objects, but here we specifically use the term to refer to systems for which fundamental properties may be directly determined. Pinfield et al. (2006) highlighted the value of systems where the age and composition of substellar objects can be independently determined, e.g., from a stellar or white dwarf companion, and Liu et al. (2008) described an equivalent use of systems with dynamical mass measurements. Essentially, since brown dwarfs follow a mass–luminosity–age relation, the measurement of either mass or age in addition to the measured luminosity allows any other quantity to be fully specified using evolutionary models. This approach can be extremely useful, for example, by offering precise determinations of T_{eff} and $\log(g)$, which can then be compared directly to atmospheric models. Of course, the measurement of mass, age, *and* luminosity offers a direct test of evolutionary models, which is possible with HD 130948BC.

2. Observations

2.1. *HST*/ACS-HRC Coronagraph

We retrieved *Hubble Space Telescope* (*HST*) archival images of HD 130948BC obtained with the ACS High Resolution Camera (HRC) coronagraph (1''8 spot) on 2002 September 6 and 2005 February 23 UT. These data were taken as part of engineering programs to test the stability of the PSF of an occulted star between orbits (ENG/ACS-10445, PI Cox) and to measure the coronagraphic PSF as a function of wavelength (CAL/ACS-9668, PI Krist). Fortunately, the scientifically interesting bright star HD 130948A was selected to perform these tests. At both epochs, HD 130948BC is tight enough that the PSFs of the two components are significantly blended with each other. Therefore, to determine the relative astrometry we fit all six parameters (x , y , and flux for both components) simultaneously with an iterative, χ^2 -minimum-finding approach. Similar to our previous work (Liu et al. 2008), we used TinyTim (Krist 1995) to model the off-spot PSFs of the binary components and the `amoeba` algorithm (e.g., Press et al. 1992) for minimum finding in the six-dimensional parameter space.

One challenge in obtaining precision astrometry for HD 130948BC is the removal of background light from the primary, which is only 2''6 away. Though most of the light from HD 130948A is occulted by the 1''8 coronagraph spot, the remaining light reaching the detector is highly structured and wavelength-dependent. The most effective technique for removal of the light from the occulted primary star is to use an image taken at the same epoch but at a different telescope roll angle. This way, the background due to the bright primary remains more or less unchanged while any other objects in the field move to a different part of the image. As part of the 2005 engineering tests, images were taken at two different roll angles, so the background subtraction for these data is straightforward. However, all of the engineering data from 2002 were taken at the same roll angle, so data from a different epoch but the same filter must be used for the background subtraction. For the 2002 *F850LP* data, we were able to use the PSF of HD 130948A itself because the 2005 engineering data were taken in this filter. However, the remainder of the 2002 data were taken with the linear ramp filter *FR914M*, and HD 130948A was never imaged in this filter on any other occasion. Due to the wavelength dependence of the background, we must use an occulted star of similar spectral type to subtract the background. Although very few *FR914M* coronagraph data are available in the archive, one star of identical spectral type, α Cen A (G2V), has been observed in *FR914M*. The α Cen ramp filter data were not taken at exactly the same nearly-monochromatic wavelengths as our science images, so we used the two α Cen images which bracketed our science data to create two different background-subtracted images of HD 130948BC in *FR914M*. Though the resulting background subtractions were not very different, in the end, we only used the subtraction that yielded a lower χ^2 in the PSF-fitting of HD 130948BC. When performing any background subtraction, the images were first optimally shifted and scaled to the nearest 1 pixel and 1% in normalization by minimizing the RMS of the subtraction residual of the central 200×200 -pixel region of the detector (this region excludes HD 130948BC). The final background-subtracted images of

HD 130948BC are shown in Figure 1. The lack of visible structure in the background demonstrates that the PSF from HD 130948A was adequately subtracted.

For PSF-fitting of the background-subtracted images, TinyTim PSF models were generated to the specifications of the data. PSFs were created for detector locations within the nearest pixel of HD 130948BC (this is important because of the field dependence of the geometric distortion that shapes the PSF). We used the optical spectrum of the L4 dwarf 2MASS J0036+1821 from Reid et al. (2001) as the spectral template for PSF generation. We included different amounts of telescope jitter (0 to 20 mas in 5 mas steps) and telescope defocus (-20 to $+20$ μm in 4 μm steps) to simulate the effect of “breathing” on the PSF.¹ We generated finely sampled PSFs at $5\times$ the native pixel scale so that we could accurately interpolate them to a fraction of a pixel. We used the distortion solution of Anderson & King (2004) to correct the best-fit positions for the severe geometric distortion of the ACS, and we used their measured ACS pixel scale, which was derived by comparing commanded (POSTARG) offsets of *HST* in arcseconds to the resulting pixel offsets. They derived two such pixel scales for two epochs of observations of 47 Tuc, and we adopt the mean and standard deviation of these two: 28.273 ± 0.006 mas/pix.

Rather than simply use the scatter of individual measurements to estimate the astrometric uncertainty, we performed Monte Carlo simulations in order to quantify potential systematic errors in our PSF-fitting routine. Typically, the most important source of systematic error would be the imperfect modeling of the PSF, but for HD 130948BC the imperfect subtraction of the background light due to HD 130948A may also be significant. This is because the structured background light will change even within a single orbit due to thermal changes which affect the telescope optics (e.g., the well-known “breathing” phenomenon). Also, the coronagraphic occulting spot must be stowed when not in use, and each time it is deployed it will be in a slightly different position, which will change the background slightly, but noticeably. It is easy to imagine how lumps in the residual background structure resulting from an imperfect subtraction could confuse measurement of both the astrometry and the flux ratio. In Appendix A, we describe in detail our Monte Carlo simulations, from which we derived measurement offsets and uncertainties in our PSF-fitting procedure for *HST*/ACS images. The offsets ranged in amplitude from 0.1–0.8 mas in separation, 0.1–0.7° in PA, and 0.01–0.05 mag in flux ratio. The offsets are comparable in size to the uncertainties predicted by the Monte Carlo simulations, which are also comparable in size to the RMS scatter among the individual measurements. The simulations showed that systematic errors (i.e., imperfect PSF-modeling) dominate the predicted uncertainties. The best-fit positions and flux ratios from both epochs, with offsets applied and uncertainties adopted from the Monte Carlo simulations, are given in Table 1.

¹“Breathing” is the term which has come to be used to describe the change in telescope focus due to thermal effects, especially within one pointing. TinyTim parameterizes this as the offset between the secondary and primary mirrors of the telescope relative to the nominal in μm . TinyTim also allows for different amounts of Gaussian telescope jitter due to guiding.

2.2. Keck NGS AO

On 2007 January 26 UT, we began monitoring HD 130948BC using natural guide star adaptive optics (NGS AO) at the Keck II Telescope on Mauna Kea, Hawaii. The seeing conditions on that night were relatively poor; however, at five subsequent epochs we obtained superior NGS AO imaging data. We used the facility IR camera NIRC2 with its narrow field-of-view camera, which produces $10''.2 \times 10''.2$ images. The primary star HD 130948A ($R = 5.5$ mag; Monet et al. 2003) located $2''.6$ away from HD 130948BC provided the reference for the AO correction. Table 2 summarizes our Keck NGS observations, and typical images are shown in Figure 1.

At each epoch, HD 130948BC was imaged in one of the filters covering the standard atmospheric windows from the Mauna Kea Observatories (MKO) filter consortium (Simons & Tokunaga 2002; Tokunaga et al. 2002). We initially obtained data in the K -band filter, though we subsequently took data in J -, H -, K_S -, and K_{cont} -band ($\lambda_c = 2.271 \mu\text{m}$, $\Delta\lambda = 0.030 \mu\text{m}$).

On each observing run, we obtained dithered images, offsetting the telescope by a few arcseconds between every 1–3 images. There was no need to exclude any of the images at any epoch on the basis of poor image quality. The images were reduced in a standard fashion. We constructed flat fields from the differences of images of the telescope dome interior with and without continuum lamp illumination. Images were registered and stacked to form a final mosaic, though all the results described here were based on analysis of the individual images.

For the 2008 March and April epochs, we also obtained unsaturated images of the primary HD 130948A interlaced with deep exposures in which it was saturated but HD 130948BC was measured at high S/N . The minimum integration time of NIRC2 is set by the sampling mode (e.g., single or correlated double sampling) and how much of the array is read out, so by using a very restricted subarray we achieved exposures of 4.372 ms (512×32) and 2.968 ms (384×24).

We used the unsaturated images of the primary to estimate the Strehl ratio and FWHM of images from the 2008 March and April epochs. Since no field stars were available to obtain a simultaneous measurement of the Strehl ratio and FWHM in images from other epochs, we used images of HD 130948BC itself. The FWHM was determined by a Gaussian fit to the core of the PSF of HD 130948B. The quantities needed to calculate the Strehl ratio were obtained as follows: (1) the peak flux of the science PSF was determined by a Gaussian fit to the core of the PSF of HD 130948B after removing contaminating flux from HD 130948C by subtracting the science image from itself after being rotated by 180° about HD 130948C; (2) the total flux of HD 130948B was measured using aperture photometry of HD 130948BC, then correcting for binarity using the measured flux ratio for that epoch and filter; (3) the peak-to-total flux ratio of the theoretically perfect PSF was determined using the publicly available IDL routine `NIRC2STREHL`² using the same aperture size as was used for the science image. We report the mean and standard deviation of the

²<http://www2.keck.hawaii.edu/optics/lgsao/software/nirc2strehl.pro>

Strehl ratio and FWHM measured for each set of dithered images at each epoch in Table 2.

We computed the expected relative shift of the two components of HD 130948BC at each epoch due to differential chromatic refraction (DCR). Even though B and C have nearly identical spectral types based on resolved spectroscopy, small color differences can change the extent to which the atmosphere refracts their light, thus changing their relative position as a function of airmass. We used the prescription of Monet et al. (1992) for the effect of DCR, and we used the prescription of Stone (1984) for the index of refraction of dry air as a function of wavelength. Thus, given the effective wavelength of each component and details of the observations (coordinates of HD 130948BC, time observed, and observatory latitude), we calculated the expected shift due to DCR. We computed the effective wavelengths of B and C using template spectra of an L3 object (2MASS J1146+2230AB; Cushing et al. 2005) and an L5 object (SDSS J0539-0059; Cushing et al. 2005) to represent the extremes of the possible spectral difference between the two components of HD 130948BC (each is $L4\pm1$). The resulting effective wavelengths for K -band were $2.1976\ \mu\text{m}$ and $2.1939\ \mu\text{m}$ for L3 and L5, respectively. Even given this large allowance for spectral differences between the two components of HD 130948BC, the DCR offset is typically an order of magnitude smaller than the error at any given epoch. (The largest estimated offset is 0.5σ for the 2008 April observations taken at airmass 1.6.) Therefore, we are justified in ignoring the effects of DCR in the relative astrometry.

To determine the relative positions and fluxes of HD 130948BC, we used a simple analytic representation of the PSF to deblend the two components. The model was the sum of three elliptical Gaussians in which each Gaussian component was allowed to have a different FWHM and normalization, but all components had the same ellipticity and semimajor axis PA. In the vicinity of HD 130948BC there is a significant contribution of both sky background and light from the bright primary HD 130948A. Therefore, we also simultaneously fitted a sloped, flat surface to account for the flux not due to HD 130948BC. In all, we fitted simultaneously for 16 parameters: 6 parameters for the positions and fluxes of HD 130948BC, 7 parameters for the three-component elliptical Gaussian model, and 3 parameters for background light due to HD 130948A and the sky. The best-fit parameters were found by a Levenberg-Marquardt least-squares minimization in which all pixels were weighted equally. Our fitting procedure yielded a set of measurements of the projected separation, PA, and flux ratio for HD 130948BC. We applied the distortion correction developed by B. Cameron (priv. comm.) to the astrometry, which changed the results well below the 1σ level.

The internal scatter of the measurements at each epoch was very small, but this does not include systematic errors due both to the imperfect modeling of the PSF and to the temporally varying and spatially structured background light. To quantify these systematic errors, we conducted extensive Monte Carlo simulations designed to replicate the observations at each epoch. These simulations are described in detail in Appendix B. By comparing the input to fitted parameters for 10^3 simulated images, we determined the offset and uncertainty appropriate for each epoch. The offsets ranged in amplitude from 0.1–0.7 mas in separation, 0.03–0.20° in PA, and

0.001–0.1 mag in flux ratio. We applied these offsets and although they could be up to $1\text{--}3\sigma$, their application only changed the resulting total mass of HD 130948BC by only 0.2σ . It also improved the reduced χ^2 of the best-fit orbit significantly, from a reduced χ^2 of 1.8 to a reduced χ^2 of 1.1. The uncertainties predicted by the simulations were up to $3\times$ larger than the RMS scatter among individual measurements at each epoch.

For the 2008 March and April epochs, we used the interlaced unsaturated images of the primary HD 130948A in a different approach for measuring the relative astrometry and flux ratio of HD 130948BC. We extracted 40×80 -pixel cut-outs of HD 130948A from the short exposures and HD 130948BC from the deeper exposures. We then stitched together these cut-outs, pairing an image of HD 130948BC with each of the images of HD 130948A taken immediately before and after it. We employed the StarFinder software package (Diolaiti et al. 2000) to iteratively solve for the PSF, positions, and fluxes of the three components in these combined images. Unfortunately, the Keck AO system did not keep HD 130948A sufficiently fixed on the NIRC2 array (it drifted up to ~ 10 mas between deep exposures) to enable the measurement of the positions of B and C relative to A from our data. Since we used every available independent PSF contemporaneous with the observations in measuring the system properties, we did not verify this empirical PSF-fitting approach directly by testing StarFinder on simulated binary images. However, at the 2008 April epoch, we obtained standard full-frame (1024×1024) images, which we have analyzed and simulated in the same fashion as data from the previous epochs using our simple analytic model of the PSF. The measured relative astrometry and flux ratio are consistent using both approaches. In fact, the separation measured using our simple analytic PSF model, which is more likely to be affected by systematic errors, would be 3σ discrepant with the StarFinder empirical PSF results if the offset derived from simulated binary images was not applied. This suggests that our Monte Carlo simulations accurately predict measurement offsets for the analytic PSF approach, and that the StarFinder empirical PSF-fitting approach does not harbor any significant systematic errors.

By interlacing short and deep exposures, we were able to measure the photometric stability during each data set, thus enabling the measurement of the absolute photometry of HD 130948BC by finding the fluxes of B and C relative to A. Photometry of HD 130948A is contained in the 2MASS Point Source Catalog (Cutri et al. 2003), and we neglect the small terms needed to convert the 2MASS photometry to the MKO system for a G2 star (~ 0.003 mag). Because HD 130948A is very bright with blue *JHK* colors, it is unsaturated only in short 2MASS exposures (51 ms) taken in *K*-band, thus, the quality of the 2MASS photometry is best in *K*-band (0.02 mag uncertainty) and very poor in *J*- and *H*-band (0.2 mag uncertainty). To eliminate the need to rely on 2MASS *J*- and *H*-band photometry, we used *J* – *K* and *H* – *K* colors to tie our *J*- and *H*-band photometry to the higher quality *K*-band 2MASS photometry. We computed synthetic photometric colors of $J - K = 0.339\pm 0.010$ mag and $H - K = 0.057\pm 0.010$ mag from a low-resolution spectrum of HD 130948A which we obtained using the IRTF spectrograph SpeX (Rayner et al. 1998) on

2008 May 16 UT³. The spectra were reduced using the SpeXtool software package (Vacca et al. 2003; Cushing et al. 2004). Our adopted uncertainties in the synthetic colors are the typical error in determining the continuum slopes of FGK stars from J - to K -band using SpeX (Rayner, Cushing, & Vacca 2007, in prep.). To determine the uncertainty in the photometry of HD 130948BC, we added in quadrature: (1) the error in the K -band 2MASS photometry of HD 130948A; (2) the error in the synthesized $J - K$ or $H - K$ color of HD 130948A; (3) the standard error of the mean relative flux measured in the stitched-together images (i.e., the RMS scatter divided by \sqrt{N} , where N is the number of deep exposures given in Table 2), which is dominated by the uncertainty in deblending the B and C components; and (4) the RMS scatter in the measured flux of HD 130948A from our NIRC2 image sequence (a direct measure of the photometric stability over the entire data set). Our photometry is consistent with that previously reported by Potter et al. (2002) but with much smaller errors in J - and K -band.

In Table 2, we present the mean of the relative astrometric and photometric measurements at each epoch as determined from the two PSF-fitting procedures described above. For cases in which the analytic model of the PSF was used (prior to 2008 March), offsets have been applied and uncertainties adopted from our Monte Carlo simulations. For the remaining cases, in which StarFinder empirical PSF-fitting was used, the quoted uncertainty is the RMS scatter of the measurements for individual images. In Table 3, we present our photometry for all three components of HD 130948ABC.

2.3. Gemini Hokupa‘a AO

As described by Potter et al. (2002), the discovery images of HD 130948BC were obtained using the Hokupa‘a curvature AO system on the Gemini North Telescope, on Mauna Kea, Hawaii. Hokupa‘a observations were carried out over a period of approximately 14 months beginning on 2001 February 24 UT. We retrieved all available raw data from the CADC Archive (GN-2001A-DD-2, GN-2001A-C-24, GN-2001B-DD-1, GN-2002A-DD-1). This included four epochs of dual-beam imaging, which employed a Wollaston prism to simultaneously obtain orthogonally polarized images, as well as two epochs of normal imaging in which the Wollaston prism was not employed. The Wollaston prism data were originally used to search for circumstellar material around HD 130948A using simultaneous difference imaging. The nominal instrument platescale, with or without the Wollaston prism, is 19.98 ± 0.08 mas/pix.

We used the same PSF-fitting procedure as described for the Keck NGS images on the Gemini data, which we registered and cosmic-ray rejected. As judged from the FWHM of the best-fit PSF model, the image quality was best on 2001 February 24 and 2001 June 28 UT. Simultaneous dual-

³The spectrum of HD 76151 (G2V; Rayner, Cushing, & Vacca 2007, in prep.) publicly available in the IRTF Spectral Library (<http://irtfweb.ifa.hawaii.edu/~spex/WebLibrary/>) yielded consistent synthetic colors.

beam images from 2001 February 24 yielded inconsistent astrometry at the 2σ level (0.7 mas) in separation and the 6σ level (1.2°) in PA, where these confidence limits correspond to the internal scatter of the set of measurements taken in each beam. This inconsistency suggests that there are significant systematic errors that affect the PSF, platescale, and/or optical distortion of each orthogonally polarized beam differently. As there is no way to effectively quantify these systematic errors, we favor the use of the 2001 June 28 epoch images, which did not use the Wollaston prism and are of comparable image quality (FWHM ≈ 75 mas in H -band) to the 2001 February 24 data. On 2001 June 28, the separation and PA measured by our PSF-fitting procedure were 129.0 ± 1.3 mas and $318.6 \pm 0.5^\circ$, respectively. We refer to this as the “measured” astrometry hereinafter. This astrometry is consistent with the 134 ± 5 mas separation and $317 \pm 1^\circ$ PA reported by Potter et al. (2002) as the “average” astrometry for the time period of 2001 February 24 to 2001 September 20 UT.

As an additional check, we also extracted the astrometry presented by Potter et al. (2003) in their Figure 3. (The raw astrometry was not published in that conference proceedings.) They presented four epochs spanning 2001 February 24 to 2002 April 23 UT, over which the separation changes from 130.9 to 107.7 mas and the PA changes from 313.5 to 307.7° . We refer to this as the “extracted” astrometry hereinafter. The separation range is consistent with what we measured from the archival data, but the PA range is clearly inconsistent with the PA we measured directly from the archival data (and the PA reported by Potter et al. 2002). The $\approx 5^\circ$ discrepancy in the PA could be explained if the orientation of the detector on the sky was not correctly recorded in the header of the archival data. Indeed, this seems likely to be the case because all archival data we retrieved record the same value for the orientation of the detector (i.e., zero) even when the rotator had obviously been changed by $\approx 90^\circ$ for images taken at the same epoch. However, this explanation fails to account for the inconsistency between the PAs reported by Potter et al. (2002, 2003).

Archival images of the binary Gl 569Bab taken on 2001 February 24 UT using the same instrumental setup as the contemporaneous HD 130948BC data (i.e., dual-beam Wollaston prism mode) offer strong evidence for the sky orientation not being stored correctly in the header. We measured a PA of $70 \pm 3^\circ$ for Gl 569Bab, whereas the ephemeris of Simon et al. (2006) predicts a PA of 314° at that epoch (a 116° systematic offset!). We also measured the separation of Gl 569Bab to be 88 ± 2 mas, which is discrepant with the ephemeris prediction of 84 mas by 2σ . This supports our suspicion of a systematic error in the platescale of the instrument in Wollaston prism mode that motivated us to use non-Wollaston images for our “measured” astrometry.

In the next section, we will consider both possible sets of Gemini astrometry, “extracted” versus “measured”, when determining the orbit of HD 130948BC. However, our default orbit solution uses only the *HST* and Keck astrometry.

3. Dynamical Mass Determination

3.1. Orbit Fitting using Markov Chain Monte Carlo

The orbit of HD 130948BC is quite well constrained as our observations cover $\sim 70\%$ of the orbital period. However, in order to search for the influence of parameter degeneracies in our orbit fit and determine robust confidence limits on the orbital parameters, we used a Markov Chain Monte Carlo (MCMC) technique (e.g., Bremaud 1999) for orbit fitting, in addition to a gradient descent technique. In short, the MCMC method constructs a series of steps through the model parameter space such that the resulting set of values (the “chain”) is asymptotically equivalent to the posterior probability distribution of the parameters being sought. The code that performed the MCMC fit is described in detail in the study of 2MASS J1534–2952AB by Liu et al. (2008). Chains all had lengths of 2×10^8 , and the correlation length of our most correlated chain, as defined by Tegmark et al. (2004), was 4.2×10^4 for the orbital period, with equal or smaller correlation lengths for other orbital parameters. This gives an effective length of the chain of 6.5×10^3 , which in turn gives statistical uncertainties in the parameter errors of about $1/\sqrt{6.5 \times 10^3} = 1.2\%$, i.e., negligible. We used uniform priors in period (P), semimajor axis (a), PA of the ascending node (Ω), argument of periastron (ω), and time of periastron passage (T_0). We used a prior in inclination proportional to $\sin(i)$ (i.e., random orbital orientation) and an eccentricity prior of $f(e) = 2e$ (e.g., see Duquennoy & Mayor 1991).

As an independent verification of our MCMC results, we also fit the orbit of HD 130948BC using the linearized least-squares routine `ORBIT` (described in Forveille et al. 1999). We give the resulting orbital parameters and their linearized uncertainties in Table 4. All of the orbital parameters are consistent between the `ORBIT` and MCMC results. In fact, they are all consistent to much better than 1σ , which is expected since both orbit-fitters should find the same χ^2 minimum in parameter space (i.e., the two methods are applied to the same dataset). The reduced χ^2 of the `ORBIT` solution was 1.14 (identical to the MCMC solution), and the total mass was $0.108 \pm 0.002 M_\odot$, which includes the error in the parallax and is also consistent with the MCMC-derived mass.

3.2. Fitting Results

Figure 2 shows the resulting MCMC probability distributions for the seven orbital parameters of HD 130948BC, most of which are somewhat non-Gaussian. The two distributions that are most nearly Gaussian and particularly well-constrained are the inclination and the PA of the ascending node (Ω), the latter of which along with ω actually have a 180° ambiguity without radial velocity information. The best-fit parameters and their confidence limits are given in Table 4, and the best-fit orbit is shown in Figure 5. The reduced χ^2 of the orbital solution is 1.14.

Applying Kepler’s Third Law to the period and semimajor axis distributions gives the posterior probability distribution for the total mass of HD 130948BC, with a median of $0.1085 M_\odot$, a standard

deviation of $0.0018 M_{\odot}$, and 68(95)% confidence limits of ${}^{+0.0019}_{-0.0017}({}^{+0.004}_{-0.003}) M_{\odot}$ (Figure 4). The MCMC probability distribution of the total mass does not include the uncertainty in the parallax (0.44%), which by propagation of errors contributes an additional 1.3% uncertainty in mass. Since the MCMC-derived mass distribution is asymmetric, we account for this additional error by randomly drawing a normally distributed parallax value for each step in the chain, which we then used to compute the distance and total mass. The resulting mass distribution is indistinguishable from Gaussian (Figure 4). Our final determination of the total mass is $0.109 \pm 0.002({}^{+0.005}_{-0.004}) M_{\odot}$ at 68(95)% confidence. Thus, the total mass of this system is determined to 2% precision.

The total mass is determined to a much higher precision than would be calculated directly from the uncertainties in the orbital period and semimajor axis because these two orbital parameters are strongly correlated (Figure 3). This is essentially a consequence of encoding Kepler’s Second Law (equal area per unit time) in the orbit fitter, so that it naturally determines the ratio a^2/P quite well. Thus, the correlation between a and P roughly follows lines of constant mass since M_{tot} is just $(a^2/P)^2/a$. This property of orbit determination is well-known and has often been utilized to measure dynamical masses even when the orbital parameters are not well-constrained (e.g., Schaefer et al. 2003).

3.3. Including Gemini Astrometry

Our default best-fit orbit presented above includes only the *HST* and Keck measurements of HD 130948BC. In section §2.3, we discussed the different Gemini measurements of HD 130948BC and their inconsistencies. The Gemini measurements have the potential to improve the orbit determination by extending the observational time baseline, so we explored the effect of adding each of these two different measurements by running two additional MCMC chains. One chain uses the Gemini astrometry we extracted from Potter et al. (2003) for the 2001 February 24 UT epoch, and the other chain uses the Gemini astrometry we measured directly from archival images at the 2001 June 28 UT epoch (this astrometry is consistent with that presented by Potter et al. 2002). For our “extracted” measurement, we estimated uncertainties of 2 mas in separation and 1° in PA. The MCMC chain with the addition of our “extracted” measurement yielded a similar reduced χ^2 (1.05) to our default chain, and the orbital parameters were generally better constrained (e.g., Figure 7 shows that the posterior mass distribution was somewhat tighter). But the MCMC chain with the addition of our “measured” Gemini astrometry had an unacceptably large reduced χ^2 (14.7), and the resulting orbital parameters were generally inconsistent with our default chain. The PA of the “measured” Gemini point is grossly inconsistent with any best-fit orbit: for instance, the binary must revolve backwards (with respect to the Keck and *HST* data) to be consistent with the “measured” Gemini point (Figure 6). In other words, the “measured” Gemini astrometry is inconsistent with any physically plausible orbit that is also consistent with the *HST* and Keck astrometry. Thus the inconsistencies between the “extracted” and “measured” astrometry discussed in §2.3 seem to be due to a large systematic error in the PA of the “measured” Gemini astrometry

(e.g., due to an incorrectly recorded orientation of the detector). While our “extracted” astrometry seems to improve the orbit determination, we conservatively exclude it from our default orbital solution as we have no way to accurately quantify its astrometric uncertainties.

4. Age of the Primary HD 130948A

Age determinations for individual main-sequence field stars are challenging and imperfect. Estimates generally rely on the slowing of the stellar rotation period as stars grow older (Skumanich 1972). Stars spin down as they age because stellar winds carry away angular momentum; the slower rotation periods then lead to a decline in stellar activity due to the underlying stellar dynamo.

Gaidos (1998) assigned an age range of 0.2–0.8 Gyr to characterize his young solar-analog sample, of which HD 130948A is a member. Given the importance of the system’s age in interpreting our mass measurement of the brown dwarf binary, we examine here the specific properties of HD 130948A to refine the age estimate.

4.1. Chromospheric Activity

For solar-type stars, chromospheric activity as traced by Ca II HK emission provides one method to estimate ages. Donahue (1993, 1998) provide a calibration for this index:

$$\log(t) = 10.725 - 1.334R_5 + 0.4085R_5^2 - 0.0522R_5^3 \quad (1)$$

where t is the age in years and $R_5 = 10^5 R'_{HK}$, valid for $\log(R'_{HK}) = -4.25$ to -5.2 . Henry et al. (1996) and Wright et al. (2004) measure $\log(R'_{HK}) = -4.45$ and -4.50 for HD 130948A, respectively, which translate into ages of 0.6 and 0.9 Gyr. A clear error estimate is not available for this relation.

Mamajek & Hillenbrand (2008) have updated this relation, incorporating new samples of Ca II HK data, revised ages and membership lists for nearby open clusters, and corrections for trends in activity with stellar color (mass). Their relation differs most notably from the Donahue one at the youngest ages ($\lesssim 0.1$ Gyr). They find:

$$\log(t) = -38.053 - 17.912 \log(R'_{HK}) - 1.6675 \log(R'_{HK})^2. \quad (2)$$

The resulting implied ages for HD 130948A are 0.4 and 0.6 Gyr for the aforementioned $\log(R'_{HK})$ values. Mamajek & Hillenbrand (2008) estimate errors of ≈ 0.25 dex in the age ($\approx 60\%$), based on the dispersion produced by their relation when applied to binary stars and star clusters. We adopt an age from this method of 0.5 ± 0.3 Gyr.

Direct comparison to the open cluster data used by Mamajek & Hillenbrand (2008) provides useful reference points. The Hyades (625 Myr; Perryman et al. 1998) provides the most populous

sample for comparison; the cluster’s median $\log(R'_{HK}) = -4.47 \pm 0.09$ (68% confidence range) is very well-matched to HD 130948A. The slightly younger UMa (500 Myr; King et al. 2003) and Coma Ber (600 Myr; King & Schuler 2005) clusters also have comparable values of -4.48 ± 0.09 and -4.43 (no confidence limits given), respectively, though with much smaller samples of stars.⁴ The data for HD 130948A are clearly inconsistent with older clusters NGC 752 (2 Gyr; Dinescu et al. 1995) and M 67 (4 Gyr; Sarajedini et al. 1999; VandenBerg & Stetson 2004) that have $\log(R'_{HK})$ values of -4.70 and -4.84 ± 0.11 , respectively. However, the activity data for HD 130948A are still formally consistent with ages as young as the Pleiades (-4.33 ± 0.24), given the large scatter in the sample for that cluster.

4.2. X-Ray Emission

X-ray emission of solar-type stars also declines with age. Hünsch et al. (1999) measure $\log(L_X) = 29.0$ dex (cgs) for HD 130948A with a 7% uncertainty. Gaidos (1998) provides an age calibration based on scaling relations for stellar activity:

$$\log(L_X/L_{\text{bol}}) = -6.38 - 2.6\alpha \log(t_9/4.6) + \log[1 + 0.4(1 - t_9/4.6)] \quad (3)$$

where t_9 is the age in Gyr and α is the coefficient that relates rotation period to stellar age, either $\alpha = 0.5$ (Skumanich 1972) or $\alpha = 1/\exp$ (Walter & Berry 1991). Following Wilson et al. (2001), we adopt the zero-point of -6.38 based on the X-ray luminosity of the Sun from Maggio et al. (1987). Adopting the $L_{\text{bol}}/L_{\odot} = 1.21$ from Gaidos (1998) gives $\log(L_X/L_{\text{bol}}) = -4.70$ for HD 130948A, which corresponds to an estimated age of 0.1–0.3 Gyr, depending on the value of α .

Mamajek & Hillenbrand (2008) find that X-ray emission is strongly correlated with $\log(R'_{HK})$, and they derive a relation between X-ray activity and age from this correlation and their relation between chromospheric activity and age:

$$\log(t) = 1.20 - 2.307 \log(L_X/L_{\text{bol}}) - 0.1512 \log(L_X/L_{\text{bol}})^2 \quad (4)$$

where t is the age in years. This relation gives an age of 0.5 Gyr for HD 130948A, which perhaps not surprisingly is in agreement with the age estimate from their chromospheric activity relation (Equation 2). This agreement indicates that HD 130948A shows typical X-ray emission given its chromospheric activity level.

As a more direct point of reference, the X-ray luminosity of HD 130948A is in excellent agreement with single G stars in the Pleiades and Hyades, where the average values are 28.9–29.0 (Stern et al. 1995; Stelzer & Neuhäuser 2001). Unfortunately, there is only a modest difference in the distribution of X-ray luminosities for G stars in these two clusters (e.g., Preibisch & Feigelson 2005).

⁴Note that the ages for these latter two clusters are older than adopted in the Donahue analysis. Combined with the larger sample of young clusters, the behavior of the activity–age relation from Mamajek & Hillenbrand (2008) produces the somewhat younger age for HD 130948A compared to (Donahue 1998).

Similarly, Kastner et al. (2003) have noted that the character of stellar X-ray emission changes with age, with older stars having softer *ROSAT* X-ray emission. The *ROSAT* X-ray hardness ratios *HR1* and *HR2* for HD 130948A are -0.34 ± 0.07 and -0.08 ± 0.012 , respectively (Voges et al. 1999), values which are in good agreement with G stars in the Hyades and largely distinct from young moving group members (≈ 10 – 30 Myr) and nearby (old) stars. Overall, the X-ray data for HD 130948A support an age around the Pleiades and Hyades clusters (i.e., 125–625 Myr) but do not provide a more definitive age estimate.

4.3. Rotation/Gyrochronology

Barnes (2007) proposed a method for determining the ages of solar-type main-sequence stars based on stellar rotation (“gyrochronology”). This technique is potentially the most direct and precise method for estimating stellar ages. Over a star’s lifetime, stellar winds carry away angular momentum, so the star rotates more slowly as it ages. The functional form of the spin-down was found by Skumanich (1972) to be proportional to \sqrt{t} . Barnes (2007) adds a separable color dependence, which translates to a mass dependence, to the spin-down. This is empirically motivated and suggests a mass dependence on the angular momentum loss, and thus on the strength of the stellar dynamo. In fact, his empirical relation cannot be used for all stars, but only those which share a common dynamo mechanism, one that is presumed to originate at the interface between convective and radiative zones in the stellar interior. Fully convective stars are expected to have a different dynamo mechanism that is weaker and prevents efficient spin-down, leading these stars to rotate rapidly ($P \lesssim 2$ days). This interpretation is empirically motivated by stellar rotation data which show two sequences of stars, with some stars in transition between the two states. If a main-sequence star can be shown to be part of the “interface sequence” (as almost all stars older than about 200 Myr seem to be), then its rotation period and $B - V$ color can be used to determine its age to a precision of 15–20% using the empirical gyro relation of Barnes (2007).

Gaidos et al. (2000) measured rotational modulation of HD 130948A from photoelectric time series photometry spanning 188 days. He found two distinct but similar periods of 7.69 days and 7.99 days, so we adopt the mean and standard deviation as the rotation period for HD 130948A and its uncertainty ($P = 7.84 \pm 0.21$ days). For the $B - V$ color, we adopt 0.576 ± 0.016 mag from the *Hipparcos* catalog (Perryman et al. 1997).

First, we show that we are justified in applying the Barnes (2007) relation to HD 130948A because it seems to have an interface dynamo. We have verified this in two independent ways: (1) its age-normalized rotation period (P/\sqrt{t} , where t is 0.2–0.8 Gyr, the age estimated from stellar activity indicators) and $B - V$ color place it within the “interface sequence” of stars in open clusters (see Figure 1 of Barnes 2007); and (2) its X-ray flux ($\log L_X/L_{\text{bol}} = -4.70$ from §4.2) and Rossby number (defined as $P/\tau_c = 0.29$, where τ_c is the convective turnover timescale of HD 130948A, estimated to be 27 days according to Kim & Demarque 1996) clearly place it among other X-ray active stars with interface dynamos (see Figure 1 of Barnes 2003).

The functional form of the Barnes (2007) gyrochronological age relation is:

$$\log(t) = \frac{1}{n}[\log(P) - \log(a) - b\log(B - V - c)] \quad (5)$$

where t is the age in years, P is the rotation period in days, n is the power-law exponent of the spin-down, and a , b , and c are empirical coefficients. By fitting rotation periods and colors for stars in open clusters of known ages, Barnes (2007) found coefficients of $a = 0.7725 \pm 0.011$, $b = 0.601 \pm 0.024$, $c = 0.4$ (not free to vary), and $n = 0.5189 \pm 0.0070$. We have employed the gyro relation in a Monte Carlo fashion, drawing the observational inputs and functional coefficients from normal distributions consistent with their quoted errors. This approach yields a standard deviation in the resulting age distribution consistent with the error one would obtain by propagation of errors (i.e., Equation 11 of Barnes 2007), but it preserves asymmetries in the resulting confidence limits. We thereby find a gyro age of $0.65^{+0.13(0.28)}_{-0.10(0.18)}$ Gyr for HD 130948A (68(95)% confidence limits).

Mamajek & Hillenbrand (2008) have derived new coefficients for the gyro relation that improve its agreement with observations of the Hyades, Pleiades, and the Sun: $a = 0.407 \pm 0.021$, $b = 0.325 \pm 0.024$, $c = 0.495 \pm 0.010$, and $n = 0.566 \pm 0.008$. Using these, we find a gyro age of $0.79^{+0.22(0.53)}_{-0.15(0.26)}$ Gyr for HD 130948A (68(95)% confidence limits). This is the age we adopt as the gyrochronological age of HD 130948A, despite its somewhat larger uncertainties, which stem from the larger uncertainties in the coefficients determined by Mamajek & Hillenbrand (2008). The age estimates derived using the different sets of coefficients are consistent with each other, though the improved coefficients give a slightly older age. Because of the scarcity of rotation period data for clusters, no stars older than the Hyades except the Sun were used in either calibration of the gyrochronology relation.

Comparison of HD 130948A’s properties to the stellar rotation data presented by Mamajek & Hillenbrand (2008) offers a direct assessment of its gyrochronological age. For an object of its color, it appears to be in good agreement with members of the Hyades (625 Myr; Perryman et al. 1998). In fact, its rotation period is slightly slower than the mean Hyades rotation period. This implies an age slightly older than, but marginally consistent with, the Hyades, which supports our adopting the gyro age of $0.79^{+0.22}_{-0.15}$ Gyr.

4.4. Other Age Indicators

The location on the H-R diagram relative to stellar evolutionary isochrones provides another age estimate, though for main-sequence stars this is limited since stellar luminosity changes gradually with age. Using high resolution spectroscopic data combined with bolometric magnitudes and isochrones, Valenti & Fischer (2005) derive an age estimate of 1.8 Gyr with a possible range of 0.4–3.2 Gyr. From the same data and with more detailed analysis, Takeda et al. (2007) infer a median age of 0.72 Gyr with a 95% confidence range of 0.32–2.48 Gyr.

For solar-type stars, photospheric lithium is depleted with age, as indicated from Li I $\lambda 6708$

measurements for stars in open clusters, with modest changes for $\lesssim 100$ Myr and then more rapid depletion with age. However, even within a given cluster, lithium abundances show a substantial scatter for stars of a given color (mass), and thus we consider the Li data only as a qualitative check. Measurements by Duncan (1981), Hobbs (1985), and Chen et al. (2001) give Li I $\lambda 6708$ equivalent widths of 95 ± 14 , 96 ± 3 , and 103.1 ± 3 mÅ, respectively, for HD 130948A. Compared to stars of similar $B - V = 0.58$, these values are slightly lower than the mean for the Pleiades and slightly higher than for UMa and the Hyades, though consistent with the scatter in each cluster’s measurements (Soderblom et al. 1993a,b,c).

Gaidos et al. (2000) examined the space motions of his young solar analog sample and did not associate HD 130948A with any of the known moving groups. Using his space motions, we confirm that HD 130948A does not belong to any moving groups that were identified after his analysis (Zuckerman & Song 2004; Zuckerman et al. 2006; López-Santiago et al. 2006). Thus, the space motion of HD 130948A offers no constraint on its age.

Overall, the isochrone analysis and lithium abundances are consistent with the activity-derived ages, albeit with lower precision.

4.5. Age Summary

The age estimates for HD 130948A are summarized in Table 5. The most precise estimates are derived from the connection between stellar rotation (thus activity) and age. Using gyrochronology, we have estimated the age of HD 130948A from its rotation period to be $0.79^{+0.22}_{-0.15}$ Gyr. This is consistent with the 0.5 ± 0.3 Gyr age derived from the most up-to-date relation between chromospheric activity and age (Mamajek & Hillenbrand 2008). The larger uncertainty in the activity age ($\approx 60\%$) compared to the gyro age ($\approx 25\%$) makes it somewhat less attractive, although it is better calibrated at ages intermediate between the Hyades the Sun. Less precise estimates are available from X-ray activity, lithium depletion, and stellar evolutionary isochrones, and these are all consistent with the more precise gyro age estimate.

It is important to note that the rotation data for HD 130948A are generally inconsistent with ages younger than the Hyades, so we find it unlikely that HD 130948A is much younger than ≈ 0.6 Gyr (see Figure 10 of Mamajek & Hillenbrand 2008). This assertion is free from the uncertainties in the calibration of the gyro relation at older ages, thus our 1σ (2σ) lower limits on the gyro age of 0.64 Gyr (0.53 Gyr) are expected to be reasonable. Additionally, the chromospheric activity of HD 130948A is inconsistent with stars in clusters much older than the Hyades (see Figure 4 of Mamajek & Hillenbrand 2008). Thus, the ensemble of data can be made fully consistent for an age of HD 130948A that is roughly the same as the Hyades.

In the analysis that follows, we adopt the $0.79^{+0.22}_{-0.15}$ Gyr age estimate from gyrochronology for HD 130948A, not only because it provides the best precision, but also because it is the most fundamental age indicator available. It directly probes stellar angular momentum loss, whereas

activity indicators indirectly probe the change in stellar rotation through its impact on the stellar dynamo. However, we are reluctant we caution that the gyro age still has at least two potential uncertainties: (1) the rotation period was measured over only one season and so is not completely irreproachable;⁵ (2) the gyrochronological age relation is not well-calibrated at ages older than the Hyades, as the only age datum $\gtrsim 0.6$ Gyr is the Sun. For these reasons, we will also consider the activity age of 0.5 ± 0.3 Gyr, which is less precise but is somewhat better calibrated at ages $\gtrsim 0.6$ Gyr. Future asteroseismology measurements that probe the interior structure of HD 130948A could provide an even more fundamental and precise age estimate. However, such measurements have only been obtained for a handful of very bright stars to date (Frandsen et al. 2002; Eggenberger et al. 2004; Martić et al. 2004; Carrier et al. 2005; Bouchy et al. 2005; Eggenberger & Carrier 2006).

5. Discussion

The direct measurement of the masses and/or ages of ultracool dwarfs is one of the few avenues by which theoretical models describing these objects can be tested. HD 130948BC is unique among ultracool dwarf binaries with dynamical mass determinations to date because the primary HD 130948A offers an independent age and metallicity constraint, under the conservative assumption that all three components are coeval and have the same composition. The metallicity of HD 130948A is $[M/H] = 0.00$ (Valenti & Fischer 2005), so the publicly available solar-metallicity models are well-suited to our analysis. Because the age of HD 130948A is constrained to a lower precision ($\approx 25\%$) than the total mass of HD 130948BC (2%), we have conducted the model comparisons discussed here with minimal dependence on the measured age of HD 130948A so that future improvements in the age measurement can be readily applied to our results.

In the following analysis, we utilized all available measurements of HD 130948BC: the total mass from this work; the Keck *JHK* photometry; the *Hipparcos*-measured distance; and the individual spectral types. We randomly drew the measured properties of HD 130948BC from appropriate distributions, carefully accounting for the covariance between the different quantities. For example, M_{tot} and L_{bol} are correlated through the distance (this has a small effect on our analysis), and the luminosities of the two components are correlated because the flux ratio is measured to higher accuracy than the total flux.

We have deliberately chosen to use L_{bol} rather than T_{eff} as the basis of our model comparisons because values of T_{eff} in the literature are invariably tied to either evolutionary or atmospheric theoretical models in some way. By using L_{bol} , which only depends on direct measurements of SEDs and distances, we have avoided such circular comparisons. In the following, we consider two indepen-

⁵The rotation period measured from photometric modulation due to star spots can be affected by the latitude of the spots since there is likely to be some amount of differential rotation. The fact that Gaidos et al. (2000) measured two similar but distinct rotation periods for HD 130948A highlights the difficulties in deriving a robust rotation period from time series photometry.

dent sets of evolutionary models: the Tucson models (Burrows et al. 1997) and the Lyon DUSTY models (Chabrier et al. 2000), which are appropriate for mid-L dwarfs such as HD 130948BC with significant amounts of dust in their photospheres.

5.1. Spectral Types

Potter et al. (2002) originally used resolved J -band spectra to find spectral types of dL2 \pm 2, which are on the Martín et al. (1999) system, for both components of HD 130948BC. In addition to large quoted uncertainties, this measurement suffers from systematic errors inherent to AO-fed slit spectroscopy. The quality of the AO correction is wavelength dependent, and this ultimately leads to a modification of the shape of the continuum. Since spectral typing of brown dwarfs is largely based on matching the continuum to spectral standards, this modification must be corrected first, which Potter et al. (2002) did not do.

Goto et al. (2002) determined that the spectral types of HD 130948B and C are indistinguishable by matching the H - and K -band resolved spectra with spectral templates. Before matching the spectra, they first applied an empirical correction to the continuum shape. The near-infrared spectral type of their best matching template spectrum (2MASS J0036+1821) is L4 \pm 1 (Knapp et al. 2004), and its optical spectral type is L3.5 (Kirkpatrick et al. 2000). Since the template matching was done in the near-infrared, we follow Goto et al. (2002) in adopting spectral types of L4 for both components of HD 130948BC.

In principle, the spectral template matching technique employed by Goto et al. (2002) had relative precision of 0.5 subclasses, since they compared template spectra at each integer subclass. However, we adopt an uncertainty in the spectral type of ± 1 since their method relies on a non-standard technique, and the spectra were matched in the near-infrared where the best-fitting template (2MASS J0036+1821) has a spectral type uncertainty of ± 1 . In the following analysis, we treat the errors in the spectral types of the two components as independent, such that $\Delta\text{SpT} = 0.0\pm 1.4$.

5.2. Bolometric Luminosities

We calculated the individual bolometric luminosities of HD 130948BC by using K -band bolometric corrections from the $\text{BC}_K\text{-SpT}$ relation of Golimowski et al. (2004) and our K -band absolute magnitudes. We added in quadrature the error in M_K (0.03 mag), the error resulting from the ± 1 subtype uncertainty in spectral classification (0.015 mag), and the RMS scatter in the $\text{BC}_K\text{-SpT}$ polynomial relation (0.13 mag). Thus, our derived values of L_{bol} for HD 130948BC have uncertainties of 0.05 dex (Table 6). These uncertainties may be improved by future direct measurements of the resolved SEDs of HD 130948BC, since the RMS scatter in the $\text{BC}_K\text{-SpT}$ relation dominates the errors.

The ratio of the bolometric luminosities of HD 130948BC is known more precisely than the individual values. This is because the error in the luminosity ratio does not include the error in distance and intrinsic scatter in the BC_K –SpT relation that are common to both components. We therefore combined the weighted average of our measured K -band flux ratios ($\Delta K = 0.197 \pm 0.008$ mag) with the expected difference in bolometric correction ($\Delta BC_K = 0.00 \pm 0.02$ mag; where the uncertainty is due to the independent error on the spectral type of each component) to derive a luminosity ratio of $\Delta \log(L_{\text{bol}}) = 0.079 \pm 0.008$ dex. In the following analysis, we treat the individual luminosities of HD 130948BC as correlated, in order to preserve the precision in the luminosity ratio. Thus, we are able to determine relative quantities (e.g., the mass ratio and ΔT_{eff}) to much higher precision than if we incorrectly treated the 0.05 dex uncertainties in L_{bol} as independent.

5.3. Model-Inferred Age

Brown dwarf model cooling sequences are usually thought of as predicting an observable quantity (T_{eff} , L_{bol} , etc.) from the pair of fundamental parameters mass and age. Here we have measured the total mass and individual luminosities, so we instead use these two quantities to infer the third: age. In other words, brown dwarf cooling sequences define a mass–luminosity–age relation, so the measurement of any two of these specifies the third. As suggested by Liu et al. (2008), “mass benchmarks” like HD 130948BC can offer even tighter constraints on model-inferred properties than “age benchmarks” that are more often considered in the literature.

At each model age, the individual luminosities we have measured fully determine the model-predicted individual masses. Thus, we use the evolutionary models to calculate model masses M_B and M_C as a function of age, and this yields the model-predicted M_{tot} as a function of age. We then impose the constraint of the observed M_{tot} , which uniquely determines the model age. We perform this calculation many times using randomly drawn total masses and individual luminosities to simulate the observational uncertainties while accounting for the covariance due to the distance error. The median and standard deviation of the resulting age distribution is given in Table 7. Given the very precise mass measurement (2%), the $\approx 13\%$ error on the luminosity dominates the resulting uncertainty in the model-inferred age. This procedure for inferring the age of HD 130948BC from evolutionary models is depicted in Figure 8.

The age inferred from Tucson models, $0.41_{-0.03}^{+0.04}$ Gyr, is slightly younger than inferred from the Lyon models, $0.45_{-0.04}^{+0.05}$ Gyr, though both model-inferred ages agree within the errors. The combination of theoretical models with measurements of the total mass and luminosities of HD 130948BC yields extremely small uncertainties ($\lesssim 10\%$) in the age of the HD 130948 system. The Lyon and Tucson model-inferred ages are 2.4σ and 2.2σ discrepant, respectively, with the $0.79_{-0.15}^{+0.22}$ Gyr age estimate for HD 130948A. Since the model-inferred age was derived from the observed total mass and individual luminosities of HD 130948BC, this disagreement is essentially a statement of how well (or not) models predict the luminosity evolution of objects with the masses of HD 130948BC. We discuss this discrepancy further in §5.5 and §5.8.

5.3.1. Comparison to L Dwarfs in Clusters and Moving Groups

Jameson et al. (2008) have proposed a method for estimating the ages of young ($\lesssim 0.7$ Gyr) L dwarfs for which the $J - K$ color and K -band absolute magnitude (M_K) are known. Their empirical relation is calibrated by L dwarfs in clusters and moving groups, whose ages have been determined in the literature from model stellar isochrones. Applying their empirical relation and accounting for the error in the absolute magnitudes and colors, we derive a median age and 1σ (2σ) confidence limits of $0.25^{+0.06(0.12)}_{-0.06(0.11)}$ Gyr for both components of HD 130948BC. It is worth noting that the empirical relation gives identical results for the two components even though the measured colors and absolute magnitudes of the two components are essentially independent.

The age derived from the Jameson et al. (2008) empirical relation is systematically younger by about 0.2 Gyr than the model-inferred age of HD 130948BC. This $2-3\sigma$ disagreement is perhaps not surprising since for ages older than that of the Pleiades (> 125 Myr), the empirical relation is constrained by only 3 L dwarfs in the Hyades (625 Myr) and 2 L dwarfs in the Ursa Major moving group, for which they adopt an age of 400 Myr. As discussed by Jameson et al. (2008), the age estimate of the Ursa Major moving group varies in the literature from 0.3–0.6 Gyr.⁶ We speculate that if an older age had been adopted for the Ursa Major moving group, instead of 0.4 Gyr, the empirical age relation would likely yield an older age more consistent with that inferred from evolutionary models. However, the estimated age of HD 130948A ($0.79^{+0.22}_{-0.15}$ Gyr) is even older than that inferred from evolutionary models. This creates a much larger discrepancy ($>3\sigma$) with the 0.25 Gyr age derived from the Jameson et al. (2008) empirical relation.

If HD 130948A, and thus HD 130948BC, is indeed this old, then the empirical relation would not be applicable to this system. Direct examination of the color-magnitude diagram of their sample (Figure 1 of Jameson et al. 2008) shows that the region populated by Hyades and Ursa Major L dwarfs also contains many field L dwarfs. These objects could indeed be young, or they could be older field dwarfs whose color-magnitude evolution has brought them into that region of the diagram. In fact, *all* field L dwarfs ($M_K \gtrsim 13$ mag) seem to lie in a region of the color-magnitude diagram that would imply ages intermediate between the Pleiades and Hyades. This fact and the inconsistency between our derived age and that of HD 130948A seem to highlight the danger of using this empirical age relation for L dwarfs older than its stated applicable range (<0.7 Gyr). Examination of L dwarfs with independent age estimates >0.7 Gyr would verify whether spuriously young ages can be derived for L dwarfs that are, in fact, older.

⁶For example, Mamajek & Hillenbrand (2008) adopt an age of 500 Myr for this association. Therefore, in §4.1 we have also implicitly adopted this age.

5.4. Mass Ratio and Substellarity

By measuring the relative orbit of HD 130948BC, we have determined its total mass very precisely. In order to calculate individual masses, we must infer the mass ratio ($q \equiv M_C/M_B$) from evolutionary models. Fortunately, the inferred mass ratio is very weakly dependent on theoretical models given the near-unity flux ratio of HD 130948BC (Figure 9). We calculate the mass ratio and its uncertainty from the range of model-inferred ages and the luminosity ratio. Because the ratio of L_{bol} is known to an uncertainty of 0.008 dex, theoretical models make very precise predictions of the mass ratio. The Tucson models give $q = 0.962 \pm 0.003$, and the Lyon models give $q = 0.948 \pm 0.005$. These model-inferred mass ratios are formally 2.4σ discrepant, but the resulting individual masses of HD 130948BC are completely consistent because the 2% error in the total mass dominates over the 0.3–0.5% error in the mass ratio (Table 7). If we were instead to use the age of HD 130948A ($0.79^{+0.22}_{-0.15}$ Gyr) and luminosity ratio of HD 130948BC to compute the mass ratio from the Tucson (Lyon) evolutionary models, the result would differ by $1.2^{+0.7}_{-0.5}\%$ ($1.1^{+0.9}_{-0.5}\%$). Again, the error in the total mass dominates over such small differences in mass ratio.

In principle, the mass ratio of HD 130948BC can be measured directly by future resolved observations of the radial velocities of the two components ($\Delta v_{\text{max}} = 6.4 \text{ km s}^{-1}$). Such measurements will be extremely valuable as they will test the model-predicted mass ratios, which could harbor systematic errors. However, given the attainable radial velocity precision for L dwarfs (0.1–0.3 km s^{-1} ; Blake et al. 2007), a future direct measurement of the mass ratio to 2–5% is unlikely to be precise enough to discriminate between the two sets of evolutionary models, as 0.6% errors in the mass ratio are needed to discriminate between the model-inferred mass ratios at 90% confidence level.

The individual masses of HD 130948BC inferred from theoretical models are well below the substellar boundary of $0.072 M_{\odot}$ (Chabrier & Baraffe 2000). The Tucson models give masses of $M_B = 0.0554^{+0.0012}_{-0.0013} M_{\odot}$ and $M_C = 0.0532^{+0.0012}_{-0.0011} M_{\odot}$, and the Lyon models give $M_B = 0.0558^{+0.0012}_{-0.0012} M_{\odot}$ and $M_C = 0.0528^{+0.0012}_{-0.0012} M_{\odot}$. An extremely implausible mass ratio of $\lesssim 0.5$ would be required for HD 130948B to be a star at the bottom of the main-sequence. This scenario, as well as the possibility that one component is an unresolved double, is incompatible with the near-unity flux ratio and very similar optical–near-infrared colors of the two components. Thus, both components of HD 130948BC are bona fide brown dwarfs.

5.5. Luminosity Evolution

With well-determined masses and luminosities for HD 130948BC and an independent age estimate from the primary star, we are able to directly test one of the most fundamental predictions of substellar theoretical models: the evolution of luminosity over time. Figure 10 shows the evolutionary model tracks for objects with the individual masses of HD 130948BC compared to the observations. The Tucson and Lyon evolutionary models agree very well with each other, which

is one reason why they have become trusted to estimate the bulk properties of brown dwarfs. However, both sets of models seem to disagree with the data.

Given the estimated age of $0.79_{-0.15}^{+0.22}$ Gyr, the Lyon models underpredict the luminosity of both components of HD 130948BC by a factor of 2.3 (1.6–3.4 \times , 1σ), and the Tucson models underpredict the luminosities by a factor of 3.0 (2.1–4.3 \times). There are two possible sources for the observed discrepancy in luminosity evolution. The model radii could be at fault, in which case they would have to be underpredicted by 20–45% (30–50%) by the Lyon (Tucson) models to resolve the entire discrepancy. Alternatively, the models may correctly predict the radii of brown dwarfs but underpredict their energy output. As we will see in §5.8, if the evolutionary models indeed underpredict the luminosities of HD 130948BC this has important implications for effective temperatures derived from atmospheric models.

The severe disagreement between model-predicted and observed luminosities is surprising, and we caution that it could be ameliorated by a younger estimated age. A younger age could be accommodated by most of the age indicators (Table 5), and given the challenges in estimating ages of field main-sequence stars this possibility cannot be ignored. For example, the gyro age is not beyond reproach (see §4.5), and the less precise activity age (0.5 ± 0.3 Gyr) allows for better agreement between the models and the data. However, as discussed in §4.5 our lower limit on the gyro age is expected to be robust, and HD 130948A generally appears to be very consistent with the age of the Hyades. At this age, both components of HD 130948BC would still be more luminous than predicted by evolutionary models, though the discrepancy would be on the lower end of the ranges given above. We note that Ireland et al. (2008) has observed a similar effect for GJ 802B, a substellar ($M = 0.063\pm 0.005 M_{\odot}$) companion to a kinematically old star (~ 10 Gyr), for which the evolutionary models predict an age of ~ 2 Gyr given its mass and luminosity.

5.6. Color-Magnitude Diagrams

The Lyon evolutionary models provide predictions of the fluxes in various observational bandpasses for each model mass and age. Figure 12 shows how the predicted evolution of the near-infrared flux of HD 130948BC compares to the observations. Given the age of HD 130948A ($0.79_{-0.15}^{+0.22}$ Gyr), the evolutionary models underpredict the flux in every bandpass. This is simply a reflection of the fact that Lyon evolutionary models underpredict the luminosity for both components of HD 130948BC for the age of HD 130948A. However, if ages were actually inferred from the Lyon models using the observed J -, H -, and K -band photometry, Figure 12 shows these ages would not be self-consistent. Thus model-predicted near-infrared magnitudes are internally inconsistent with the data.

In Figure 13 we show the predicted JHK colors of both components of HD 130948BC compared to the observations. The $J - K$ and $H - K$ colors are both significantly discrepant for any assumed age, while the $J - H$ colors seem to agree with the models at an age younger than we have

estimated for HD 130948A. (We do not place significant weight on this agreement as the $J - H$ color measurement has the largest uncertainty.) The general disagreement between models and data we observe on the color-magnitude diagram is not surprising since it is well-known that theoretical models do not reproduce the near-infrared colors of field L and T dwarfs very well (e.g., Knapp et al. 2004; Burrows et al. 2006).

It is interesting to note that if we were to infer the ages and masses of the components of HD 130948BC from the model $J - K$ or $H - K$ color-magnitude diagrams, we would derive masses that are $\approx 20\text{--}30\%$ smaller and ages $\approx 2\times$ younger than observed. Thus, masses and ages inferred for L dwarfs from evolutionary models and near-infrared photometry should be treated with caution.

5.7. Temperatures and Surface Gravities

Without radii measurements for HD 130948BC, we must rely on evolutionary models to derive effective temperatures and surface gravities. We have several independent measurements of the fundamental properties of HD 130948BC at our disposal to use with models to find T_{eff} and $\log(g)$: (1) the total mass of the system; (2) the individual luminosities of the two components; (3) the luminosity ratio; and (4) an independent age estimate from the primary HD 130948A ($0.79^{+0.22}_{-0.15}$ Gyr). We use the total mass (1) and individual luminosities (2) to derive T_{eff} and $\log(g)$ from the evolutionary models (Table 7). This is conceptually equivalent to using the individual masses (§5.4) and model-inferred age (§5.3) to derive T_{eff} and $\log(g)$. Unlike previous sections, it now matters significantly whether we use the model-inferred ages or the independent age from HD 130948A ($0.79^{+0.22}_{-0.15}$ Gyr) to derive the quantities of interest. We will describe the resulting differences later in this section.

The Lyon models give effective temperatures for B and C of 1990 ± 50 K and 1900 ± 50 K, while the Tucson models give systematically hotter but formally consistent temperatures of 2040 ± 50 K and 1950 ± 50 K. Since brown dwarfs cool over time, it is essentially the small range of model-inferred ages which allows the effective temperature to be predicted to a precision of 50 K. The Lyon models give surface gravities for B and C of $\log(g) = 5.143\pm 0.019$ and 5.122 ± 0.019 (cgs), while the Tucson models give systematically higher and formally inconsistent gravities of $\log(g) = 5.196\pm 0.017$ and 5.183 ± 0.017 (cgs). The precision in model-inferred surface gravity is driven by the precision in the measured total mass and near-unity mass ratio, since the radii of brown dwarfs remain nearly constant after 0.3 Gyr. Thus, the difference between the two sets of model-inferred surface gravities arises from small differences ($\approx 6\%$) in their predictions for the radii (Table 7).

5.7.1. Comparison to Field L Dwarfs

The effective temperatures we derive from evolutionary models can be compared to those which have been determined for other objects of HD 130948BC’s spectral type. L3–L5 dwarfs in the field

with L_{bol} measurements have estimated effective temperatures of 1650–2050 K. These estimates utilize the nearly flat mass-radius relationship predicted by theoretical models for brown dwarfs, adopting either a typical age (3 Gyr; Golimowski et al. 2004) or radius ($0.90 \pm 0.15 R_{\odot}$; Vrba et al. 2004) for field objects. It has been suggested that the ages of field objects are overestimated (e.g., Metchev & Hillenbrand 2006; Liu et al. 2008); however the broad range of T_{eff} estimated for field L3–L5 dwarfs is consistent with our model-inferred effective temperatures. Since both estimates are based on evolutionary models, this only means that field L3–L5 dwarfs from previous studies encompass objects of the same mass/age as HD 130948BC.

5.7.2. Comparison to Atmospheric Models

For a more interesting comparison, we consider effective temperatures derived from spectral synthesis using state-of-the-art atmospheric models. Cushing et al. (2008) have performed the most thorough spectral synthesis analysis of L and T dwarfs to date, and four of the objects in their study have near-infrared spectral types of L3–L5 (including 2MASS J0036+1821, the best matching spectral template from Goto et al. 2002). Their fits to the 0.95–14.5 μm spectra of L3–L5 dwarfs yield effective temperatures of 1700–1800 K, which are significantly cooler (150–300 K) than the evolutionary model-inferred temperatures for HD 130948BC. Adopting 1750 ± 100 K as the atmospheric model T_{eff} for the B and C components, we find the significance of the discrepancy with the Lyon (Tucson) model-inferred temperature is 2.6σ (2.1σ) for the B component and 1.8σ (1.3σ) for C. This discrepancy cannot simply be due to our adopted mass ratio because, for example, if the mass ratio were tuned so that the C component was lower mass (thus cooler) the B component would become more massive (thus hotter) and even more discrepant with the effective temperatures from spectral synthesis.

Cushing et al. (2008) also derive surface gravities for the four L3–L5 dwarfs in their study. They do so both by direct model fitting (4.5–5.5) and by using evolutionary sequences (4.9–5.5),⁷ and these ranges are consistent with our model-inferred values of $\log(g)$ for HD 130948BC.

5.7.3. Using the Age of HD 130948A

The effective temperatures we derive for HD 130948BC from the Lyon and Tucson evolutionary models depend greatly on whether we use the model-inferred ages ($0.45_{-0.04}^{+0.05}$ Gyr and $0.41_{-0.03}^{+0.04}$ Gyr, respectively) or the independent age estimate from HD 130948A ($0.79_{-0.15}^{+0.22}$ Gyr). Using the age of HD 130948A, combined with the masses of HD 130948BC, the Lyon (Tucson) models give ef-

⁷Cushing et al. (2008) fit for T_{eff} , $\log(g)$, and a normalization constant $(R/d)^2$. Thus, for the three of the four L3–L5 dwarfs with parallax measurements, they also have radius estimates. By using evolutionary models, T_{eff} and R uniquely determine $\log(g)$.

fective temperatures of 1670_{-110}^{+120} K and 1600_{-110}^{+100} K (1590_{-100}^{+110} K and 1550_{-90}^{+90} K) for the B and C components, respectively. These temperatures are 300–450 K cooler than those derived using the model-inferred age because the masses are the same, but the age used is significantly older. This disagreement is just a restatement that the model-inferred age and gyro age do not agree.

The values of T_{eff} derived using the age of HD 130948A also disagree with those determined for L3–L5 dwarfs by spectral synthesis fitting (Cushing et al. 2008). They are 100–150 K cooler than the atmospheric model temperatures.

We note that all these different sets of effective temperatures imply different radii for HD 130948BC, since the luminosities of the two components are well-determined. We consider the interplay between L_{bol} and T_{eff} in more detail in §5.8.

5.7.4. ΔT_{eff} Compared to ΔSpT

Despite the fact that the components of HD 130948BC are nearly twins in mass and spectral type, evolutionary models predict rather large differences in the effective temperatures of the two components (90 ± 7 K and 85 ± 7 K for the Tucson and Lyon models, respectively).⁸ This is computed directly from evolutionary models using the model-inferred age and measured luminosity ratio. Such a large effective temperature difference may be discernable in future spectral synthesis modeling of the resolved SED of HD 130948BC using integral field spectroscopy, which is not subject to the same difficulties as AO-fed slit spectroscopy.

We could estimate a 90 K difference in T_{eff} even without using models given the luminosity ratio and an assumption that the radii of the two components are roughly equal (i.e., $\Delta T_{\text{eff}}/T_{\text{eff}} \propto (\Delta L_{\text{bol}}/L_{\text{bol}})^{1/4}$). However, this value of ΔT_{eff} is perhaps somewhat surprising since Goto et al. (2002) found that the two components are nearly twins in spectral type, and any AO-related modifications to the continuum shape should affect both components equally. According to the SpT– T_{eff} relation of Golimowski et al. (2004), model-inferred temperatures of HD 130948BC give a difference in spectral type of ≈ 1 subtype. This lack of an apparent change in spectral type with T_{eff} may be indicative of other atmospheric processes, such as condensate cloud formation and sedimentation, playing a role that is at least as important as temperature in shaping the emergent spectra of mid-L dwarfs. In other words, this is suggestive that spectral type may not have a one-to-one correspondence with effective temperature for mid-L dwarfs (see Kirkpatrick 2005).

⁸Note that the error on the temperature difference is determined by the precision in the luminosity ratio, so it is much smaller than the 50 K uncertainties in individual values of T_{eff} .

5.8. H-R Diagram

In the previous section, we have determined various effective temperatures for HD 130948BC from evolutionary and atmospheric models given the available observational constraints. We now combine these temperatures with the observed luminosities of HD 130948BC to place both components on the Hertzsprung-Russell diagram (Figure 11). The H-R diagram shows substantial discrepancies between evolutionary models, atmospheric models, and the observations. Namely, both components of HD 130948BC are more luminous than predicted by evolutionary models for objects of their masses and effective temperatures, where T_{eff} is independently adopted from atmospheric models. Alternatively, the discrepancy in Figure 11 may be stated as both components of HD 130948BC being cooler than predicted by evolutionary models given their masses and luminosities.

The age is the least precisely determined fundamental parameter for HD 130948BC ($\approx 25\%$), since the masses and luminosities are accurate to 2% and 13%, respectively. Thus, we can consider whether changing the adopted age of the system can resolve the discrepancies between the data and models revealed in the H-R diagram. There are 3 plausible scenarios:

- If our preferred $0.79^{+0.22}_{-0.15}$ Gyr age for HD 130948A is correct, then evolutionary models underpredict the luminosities of HD 130948BC by a factor of $\approx 2-3$ (§5.5), and atmospheric models predict temperatures that are 100-150 K warmer than evolutionary models (§5.7.3).
- If the system has a slightly younger age of ≈ 0.6 Gyr, then the effective temperatures predicted by evolutionary and atmospheric models would agree. However, the evolutionary models would still underpredict the luminosities of HD 130948BC by a factor of $\approx 1.5-2$. The age in this scenario is consistent with all available age indicators (see §4.5).
- If the system is as young as ≈ 0.4 Gyr, then the evolutionary models would predict the correct luminosities. However, atmospheric models would then indicate temperatures 150–300 K cooler than predicted by evolutionary models (§5.7.2). In other words, if the actual age was consistent with the model-inferred ages of $0.45^{+0.05}_{-0.04}$ Gyr and $0.41^{+0.04}_{-0.03}$ Gyr, then the predicted and observed luminosities would agree by construction. However, the age in this scenario is significantly discrepant ($>2\sigma$) with the gyro age.

Thus, no scenario exists in which both evolutionary and atmospheric models agree with the data. In §5.5 we have already discussed the possible sources of systematic errors in evolutionary models. A number of causes might be responsible for systematic errors in the atmospheric models, including insufficient treatment of dust in the photosphere, incomplete line lists, and/or a metallicity bias in the Cushing et al. (2008) sample.

A refined age estimate for HD 130948A will be essential in discerning the source of disagreement between models and data. Another important step will be obtaining resolved spectroscopy of

HD 130948BC suitable for direct atmospheric model fitting, which will reduce the uncertainties in T_{eff} . The published AO-fed slit spectroscopy is not sufficient for this task (see §5.1), but ground-based AO integral field spectroscopy in the near-infrared and space-borne spectroscopy in the optical would be ideal once HD 130948BC is resolvable again in 2010.

5.9. Lithium Depletion

Structural models used in the prediction of brown dwarf cooling sequences make direct predictions of the amount of lithium depletion that has occurred for an object of a given mass and age. Because brown dwarfs are fully convective objects, the depletion of lithium throughout the entire object is readily detectable from observations of photospheric absorption lines, the strongest of which is the doublet at 6708 Å. Both the Tucson and Lyon models predict that objects less massive than $\approx 0.06 M_{\odot}$ never reach internal temperatures high enough to destroy significant amounts of their primordial lithium (Burrows et al. 2001; Chabrier et al. 2000). Since higher mass objects deplete lithium faster, Liu & Leggett (2005) proposed that ultracool binary systems caught at just the right point in their evolution would enable a very precise age estimate if the less massive component was found to possess lithium and the more massive component was lithium-depleted. Therefore, L dwarf binaries displaying lithium in their unresolved spectra (6 are known to date; see list in Liu & Leggett 2005) are potentially powerful systems for constraining theoretical models of brown dwarfs, since they are amenable to this “binary lithium test”.

There is no optical spectroscopy (resolved or unresolved) available for HD 130948BC to assess the presence of lithium in the system. However, the individual masses of HD 130948BC are very close to, perhaps straddling, the theoretical lithium-burning limit (Figure 14). We have determined the model-predicted lithium abundance for each component from the model-inferred age and individual masses. The Tucson models predict very little lithium depletion for both objects, with the C component having only slightly higher lithium abundance than the B component by a factor of $1.049_{-0.014}^{+0.011}$. (The error in the relative lithium abundance is dominated by the uncertainty in the model-inferred age.) On the other hand, the Lyon models predict that B is massive enough that it has depleted most of its primordial lithium ($\text{Li}/\text{Li}_0 = 0.50_{-0.23}^{+0.18}$) while C has retained most of its lithium ($\text{Li}/\text{Li}_0 = 0.83_{-0.13}^{+0.08}$). In fact, lithium burning occurs so quickly that even over the small range of Lyon model-inferred ages ($0.45_{-0.04}^{+0.05}$ Gyr) the amount of relative lithium depletion between B and C is quite uncertain (i.e., C is predicted to be richer than B by a factor of $1.6_{-0.3}^{+1.0}$).

The individual masses of HD 130948BC are such that the presence or absence of lithium in their resolved spectra would provide significant discrimination between the Tucson and Lyon models. Future resolved optical spectroscopy of HD 130948BC will provide a very sensitive, direct test of the lithium-burning limit for brown dwarfs. Given the independent age constraint from HD 130948A, the theoretical timescale for lithium burning can also be directly tested if one or both components of HD 130948BC show evidence of lithium depletion. Such direct tests of theoretical predictions for lithium burning would provide the only empirical calibration to date of often used theoretical

predictions of lithium burning in brown dwarfs. These predictions have provided the basis of the “binary lithium test”, as well as the more widely known “cluster lithium test” (e.g., Basri 1998) used to identify substellar objects among associations of a known age.

6. Conclusions

We have determined the orbit of the young L4+L4 binary HD 130948BC using relative astrometry of the system spanning 7 years of its 10-year orbital period. The astrometric measurements and their uncertainties were extensively tested through Monte Carlo simulations. The fitted orbital parameters and revised *Hipparcos* parallax give a total dynamical mass of $0.109 \pm 0.002 M_{\odot}$. The precision in mass is 2%, with nearly equal contributions to the uncertainty from the 1.7% error in the best-fit orbit and the 1.3% error in mass from the *Hipparcos* parallax error. For any plausible mass ratio, both components of HD 130948BC are unambiguously substellar. HD 130948BC has the most precise mass determination for a brown dwarf binary to date.

The primary star HD 130948A offers an independent constraint on the age of the system from various indicators: rotation, chromospheric activity, isochrone fitting, X-ray emission, and lithium depletion. The ensemble of all available age indicators is consistent with an age for HD 130948A similar to the Hyades (625 Myr). For example, its rotation period is inconsistent with ages much younger than the Hyades and its chromospheric activity is inconsistent with ages much older than the Hyades. Our preferred age estimate is $0.79^{+0.22}_{-0.15}$ Gyr, derived from the gyrochronology formalism of Barnes (2007) and Mamajek & Hillenbrand (2008).

With a measured mass, luminosity, and age, HD 130948BC provides the first direct test of the luminosity evolution predicted by theoretical models for substellar field dwarfs. Both the Tucson models (Burrows et al. 1997) and Lyon models (DUSTY; Chabrier et al. 2000) underpredict the luminosities of HD 130948B and C given their masses and age. The discrepancy is quite large, about a factor of 2 for the Lyon models and a factor of 3 for the Tucson models. In order to explain this discrepancy entirely, model radii would have to be underpredicted by 30–40%. The age of HD 130948A would need to be ≈ 0.4 Gyr younger than we have estimated in order to resolve this discrepancy. This is inconsistent with the preferred gyro age but can be accommodated by other age indicators; a more refined age estimate for HD 130948A is critically needed.

Since the mass of HD 130948BC is more precisely determined than its age, we have used the mass with the individual bolometric luminosities to infer all other properties (age, T_{eff} , etc.) from evolutionary models. We use a Monte Carlo approach to compute model-inferred quantities, and we are careful to account for covariance between the observational errors, the most notable of which is the correlation of the luminosities of the two components through their measured flux ratio. Because we use mass and L_{bol} to derive model-inferred properties, any potential systematic errors in luminosity evolution will be reflected in the model-inferred quantities. For example, the very precise model-inferred ages for HD 130948BC ($0.41^{+0.04}_{-0.03}$ Gyr from Tucson models; $0.45^{+0.05}_{-0.04}$ Gyr

from Lyon models) are self-consistent, but they are inconsistent with the independent age estimate for HD 130948A ($0.79_{-0.15}^{+0.22}$ Gyr).

Lacking measured radii for HD 130948BC, we have used evolutionary models to derive effective temperatures. Given the mass and luminosity of each component, evolutionary models predict effective temperatures of ≈ 1900 – 2000 K. Alternatively, given the mass of each component and age of the primary star, evolutionary models predict effective temperatures of ≈ 1600 – 1700 K. (The disagreement between these two temperature ranges is just a reflection of the systematic errors in luminosity evolution.) Spectral synthesis using atmospheric models gives temperatures of 1700 – 1800 K for objects of similar spectral type to HD 130948BC (L3–L5; Cushing et al. 2008). Using evolutionary models and the measured luminosity ratio gives $\Delta T_{\text{eff}} = 90$ K. Resolved spectroscopy of HD 130948B and C has previously shown that they have indistinguishable spectral types, so this rather large temperature difference may indicate that spectral type does not hold a one-to-one correspondence with T_{eff} mid-L dwarfs, even for two coeval objects. Better spectral types for the two components of HD 130948BC are needed to address this apparent discrepancy.

Comparing the different effective temperature determinations for HD 130948BC on the H-R diagram shows that the evolutionary models, atmospheric models, and observational data cannot be simultaneously brought into consistency with each other, regardless of the adopted age of the system. Thus, systematic errors in some combination of the atmospheric and/or evolutionary models are needed to explain the observed discrepancy. The best current age estimate indicates that both evolutionary and atmospheric models harbor systematic errors. Further evaluation of the disagreement between models and the data requires a refined age estimate for HD 130948A. Resolved multi-band spectroscopy of HD 130948BC is also needed to reduce the uncertainties in the atmospheric model effective temperatures by direct spectral synthesis fitting.

We also find large discrepancies when comparing the observed near-infrared colors of HD 130948BC to the Lyon models. This suggests that using color-magnitude diagrams to infer the properties of field L dwarfs from evolutionary models will lead to large errors in the resulting quantities (e.g., mass and/or age). For example, if we inferred the ages and masses of the components of HD 130948BC from the model $J - K$ or $H - K$ color-magnitude diagrams, we would derive masses that are ≈ 20 – 30% smaller than observed and ages $\approx 2\times$ younger than the age of the primary star ($0.79_{-0.15}^{+0.22}$ Gyr).

One novel aspect of using HD 130948BC to constrain theoretical models is the application of the “binary lithium test”, originally proposed by Liu & Leggett (2005). This is made possible by the fortuitous circumstance that the components of HD 130948BC are very near the mass limit for lithium burning. As a consequence, the Lyon and Tucson evolutionary models, which are almost indistinguishable in their predictions of substellar bulk properties, give very different predictions for the amount of primordial lithium remaining in the B and C components. Thus, resolved optical spectroscopy to detect the lithium doublet at 6708 \AA would provide a very discriminating test of the evolutionary models. Such a constraint is significant in that it directly tests the properties of fully convective substellar interiors (e.g., the core temperature) and/or the lithium reaction rates.

HD 130948BC is the only system currently known for which such an empirical calibration of lithium burning is possible.

Substellar theoretical models are in sore need of empirical validation as they have been employed for more than a decade to interpret observations of field dwarfs. Given the independent constraints on the age and composition provided by a stellar companion, dynamical mass measurements for triple systems like HD 130948ABC provide the most challenging tests of substellar theoretical models. However, substellar companions to stars are quite rare ($\approx 1\pm 1\%$, e.g., Oppenheimer et al. 2001; McCarthy & Zuckerman 2004; Lowrance et al. 2005; Biller et al. 2007; Lafrenière et al. 2007), and even more rare are substellar binary companions that yield dynamical mass measurements in a reasonable time frame. When the stellar companion is a bright star like HD 130948A, a wealth of additional information is available, the most important of which is a very precise *Hipparcos* distance measurement since this is the limiting factor in the precision of the dynamical mass. Stars bright enough to enable seismological measurements can yield the most stringent (10–20%) age determinations possible (e.g., Carrier et al. 2005; Bi et al. 2008). Thus, HD 130948BC represents a rare class of benchmark systems for which the most precise mass and age determinations are possible.

Our observations of HD 130948BC indicate that substellar models currently harbor significant systematic errors. The potential underestimation of L_{bol} by evolutionary models has far-reaching implications. For example, such models have been used to determine the low-mass end of the initial mass function and to predict the radii of extrasolar planets. Obtaining measurements for more systems like HD 130948BC over a broad range of mass, luminosity, and age will be critical in understanding and resolving the discrepancies that have been revealed between observations and theoretical models.

We thank Colin Cox and John Krist for their scientific foresight in selecting HD 130948A as the target for *HST* engineering and calibration observations. We also thank John Krist for assistance with the TinyTim software. We gratefully acknowledge the Keck AO team for their exceptional efforts in bringing the AO system to fruition. It is a pleasure to thank Antonin Bouchez, David LeMignant, Marcos van Dam, Randy Campbell, Al Conrad, Jim Lyke, Hien Tran, Joel Aycock, Julie Rivera, Cindy Wilburn, Jason McIlroy, and Gary Punawai and the Keck Observatory staff for assistance with the observations. We are grateful to Brian Cameron for making available his NIRC2 distortion solution, Lynne Hillenbrand for providing an advance copy of the manuscript relating chromospheric activity and age, and Adam Burrows and Isabelle Baraffe for providing finely gridded evolutionary models. We have benefitted from discussions with Michael Cushing about theoretical models, Brian Cameron about astrometry with NIRC2, Jay Anderson about astrometry with *HST*, Thierry Forveille about orbit fitting, and Hai Fu about data analysis and plotting. We also thank Zahed Wahhaj for his help with the 2007 July observations and Michael Cushing for providing us with the reduced IRTF/SpeX spectrum of HD 130948A. Our research has employed the 2MASS data products; NASA’s Astrophysical Data System; the SIMBAD database

operated at CDS, Strasbourg, France; and the M, L, and T dwarf compendium housed at DwarfArchives.org and maintained by Chris Gelino, Davy Kirkpatrick, and Adam Burgasser (Kirkpatrick 2003; Gelino et al. 2004). TJD and MCL acknowledge support for this work from NSF grant AST-0507833, and MCL acknowledges support from an Alfred P. Sloan Research Fellowship. Finally, the authors wish to recognize and acknowledge the very significant cultural role and reverence that the summit of Mauna Kea has always had within the indigenous Hawaiian community. We are most fortunate to have the opportunity to conduct observations from this mountain.

Facilities: Keck II Telescope (NGS AO, NIRC2), *HST/ACS*, Gemini-North Telescope

REFERENCES

- Anderson, J., & King, I. R. 2004, in Instrument Science Report ACS 2004-15, 1
- Barnes, S. A. 2003, *ApJ*, 586, L145
- . 2007, *ApJ*, 669, 1167
- Basri, G. 1998, in ASP Conf. Ser. 134: Brown Dwarfs and Extrasolar Planets, 394
- Bi, S.-L., Basu, S., & Li, L.-H. 2008, *ApJ*, 673, 1093
- Billler, B. A., Close, L. M., Masciadri, E., Nielsen, E., Lenzen, R., Brandner, W., McCarthy, D., Hartung, M., Kellner, S., Mamajek, E., Henning, T., Miller, D., Kenworthy, M., & Kulesa, C. 2007, *ApJS*, 173, 143
- Blake, C. H., Charbonneau, D., White, R. J., Marley, M. S., & Saumon, D. 2007, *ApJ*, 666, 1198
- Bouchy, F., Bazot, M., Santos, N. C., Vauclair, S., & Sosnowska, D. 2005, *A&A*, 440, 609
- Bremaud, P. 1999, *Markov Chains: Gibbs Fields, Monte Carlo Simulation, and Queues* (Springer-Verlag New York Inc.)
- Burrows, A., Hubbard, W. B., Lunine, J. I., & Liebert, J. 2001, *Reviews of Modern Physics*, 73, 719
- Burrows, A., Marley, M., Hubbard, W. B., Lunine, J. I., Guillot, T., Saumon, D., Freedman, R., Sudarsky, D., & Sharp, C. 1997, *ApJ*, 491, 856
- Burrows, A., Sudarsky, D., & Hubeny, I. 2006, *ApJ*, 640, 1063
- Carrier, F., Eggenberger, P., & Bouchy, F. 2005, *A&A*, 434, 1085
- Chabrier, G., & Baraffe, I. 2000, *ARA&A*, 38, 337
- Chabrier, G., Baraffe, I., Allard, F., & Hauschildt, P. 2000, *ApJ*, 542, 464

- Chen, Y. Q., Nissen, P. E., Benoni, T., & Zhao, G. 2001, *A&A*, 371, 943
- Cushing, M. C., Marley, M. S., Saumon, D., Kelly, B. C., Vacca, W. D., Rayner, J. T., Freedman, R. S., Lodders, K., & Roellig, T. L. 2008, *ApJ*, 678, 1372
- Cushing, M. C., Rayner, J. T., & Vacca, W. D. 2005, *ApJ*, 623, 1115
- Cushing, M. C., Vacca, W. D., & Rayner, J. T. 2004, *PASP*, 116, 362
- Cutri, R. M., Skrutskie, M. F., van Dyk, S., Beichman, C. A., Carpenter, J. M., Chester, T., Cambresy, L., Evans, T., Fowler, J., Gizis, J., Howard, E., Huchra, J., Jarrett, T., Kopan, E. L., Kirkpatrick, J. D., Light, R. M., Marsh, K. A., McCallon, H., Schneider, S., Stiening, R., Sykes, M., Weinberg, M., Wheaton, W. A., Wheelock, S., & Zacarias, N. 2003, 2MASS All Sky Catalog of point sources. (The IRSA 2MASS All-Sky Point Source Catalog, NASA/IPAC Infrared Science Archive. <http://irsa.ipac.caltech.edu/applications/Gator/>)
- Cutri, R. M., et al. 2000, Explanatory Supplement to the 2MASS Second Incremental Data Release
- Dinescu, D. I., Demarque, P., Guenther, D. B., & Pinsonneault, M. H. 1995, *AJ*, 109, 2090
- Diolaiti, E., Bendinelli, O., Bonaccini, D., Close, L., Currie, D., & Parmeggiani, G. 2000, *A&AS*, 147, 335
- Donahue, R. A. 1993, PhD thesis, New Mexico State University
- Donahue, R. A. 1998, in *ASP Conf. Ser. 154: Cool Stars, Stellar Systems, and the Sun*, Vol. 10, 1235
- Duncan, D. K. 1981, *ApJ*, 248, 651
- Duquennoy, A., & Mayor, M. 1991, *A&A*, 248, 485
- Eggenberger, P., & Carrier, F. 2006, *A&A*, 449, 293
- Eggenberger, P., Charbonnel, C., Talon, S., Meynet, G., Maeder, A., Carrier, F., & Bourban, G. 2004, *A&A*, 417, 235
- Forveille, T., Beuzit, J.-L., Delfosse, X., Segransan, D., Beck, F., Mayor, M., Perrier, C., Tokovinin, A., & Udry, S. 1999, *A&A*, 351, 619
- Frandsen, S., Carrier, F., Aerts, C., Stello, D., Maas, T., Burnet, M., Bruntt, H., Teixeira, T. C., de Medeiros, J. R., Bouchy, F., Kjeldsen, H., Pijpers, F., & Christensen-Dalsgaard, J. 2002, *A&A*, 394, L5
- Gaidos, E. J. 1998, *PASP*, 110, 1259
- Gaidos, E. J., Henry, G. W., & Henry, S. M. 2000, *AJ*, 120, 1006

- Gelino, C. R., Kirkpatrick, J. D., & Burgasser, A. J. 2004, *BAAS*, 205
- Golimowski, D. A., et al. 2004, *AJ*, 127, 3516
- Goto, M., Kobayashi, N., Terada, H., Gaessler, W., Kanzawa, T., Takami, H., Takato, N., Hayano, Y., Kamata, Y., Iye, M., Saint-Jacques, D. J., Tokunaga, A. T., Potter, D., & Cushing, M. 2002, *ApJ*, 567, L59
- Henry, T. J., Soderblom, D. R., Donahue, R. A., & Baliunas, S. L. 1996, *AJ*, 111, 439
- Hobbs, L. M. 1985, *ApJ*, 290, 284
- Hünsch, M., Schmitt, J. H. M. M., Sterzik, M. F., & Voges, W. 1999, *A&AS*, 135, 319
- Ireland, M. J., Kraus, A., Martinache, F., Lloyd, J. P., & Tuthill, P. G. 2008, *ApJ*, 678, 463
- Jameson, R. F., Lodieu, N., Casewell, S. L., Bannister, N. P., & Dobbie, P. D. 2008, *MNRAS*, 282
- Kastner, J. H., Crigger, L., Rich, M., & Weintraub, D. A. 2003, *ApJ*, 585, 878
- Kim, Y.-C., & Demarque, P. 1996, *ApJ*, 457, 340
- King, I. R. 1983, *PASP*, 95, 163
- King, J. R., & Schuler, S. C. 2005, *PASP*, 117, 911
- King, J. R., Villarreal, A. R., Soderblom, D. R., Gulliver, A. F., & Adelman, S. J. 2003, *AJ*, 125, 1980
- Kirkpatrick, J. D. 2003, in *Proceedings of IAU Symposium 211: Brown Dwarfs*, ed. E. Martin, 189
- Kirkpatrick, J. D. 2005, *ARA&A*, 43, 195
- Kirkpatrick, J. D., Reid, I. N., Liebert, J., Gizis, J. E., Burgasser, A. J., Monet, D. G., Dahn, C. C., Nelson, B., & Williams, R. J. 2000, *AJ*, 120, 447
- Knapp, G. R., et al. 2004, *AJ*, 127, 3553
- Krist, J. 1995, in *Astronomical Society of the Pacific Conference Series, Vol. 77, Astronomical Data Analysis Software and Systems IV*, ed. R. A. Shaw, H. E. Payne, & J. J. E. Hayes, 349
- Lafrenière, D., Doyon, R., Marois, C., Nadeau, D., Oppenheimer, B. R., Roche, P. F., Rigaut, F., Graham, J. R., Jayawardhana, R., Johnstone, D., Kalas, P. G., Macintosh, B., & Racine, R. 2007, *ApJ*, 670, 1367
- Lane, B. F., Zapatero Osorio, M. R., Britton, M. C., Martín, E. L., & Kulkarni, S. R. 2001, *ApJ*, 560, 390
- Liu, M. C., Dupuy, T. J., & Ireland, M. J. 2008, *ApJ*, in press (astro-ph/0807.0238)

- Liu, M. C., & Leggett, S. K. 2005, *ApJ*, 634, 616
- Liu, M. C., Leggett, S. K., & Chiu, K. 2007, *ApJ*, 660, 1507
- López-Santiago, J., Montes, D., Crespo-Chacón, I., & Fernández-Figueroa, M. J. 2006, *ApJ*, 643, 1160
- Lowrance, P. J., Becklin, E. E., Schneider, G., Kirkpatrick, J. D., Weinberger, A. J., Zuckerman, B., Dumas, C., Beuzit, J.-L., Plait, P., Malumuth, E., Heap, S., Terrile, R. J., & Hines, D. C. 2005, *AJ*, 130, 1845
- Maggio, A., Sciortino, S., Vaiana, G. S., Majer, P., Bookbinder, J., Golub, L., Harnden, F. R., & Rosner, R. 1987, *ApJ*, 315, 687
- Mamajek, E., & Hillenbrand, L. 2008, *ApJ*, accepted
- Martić, M., Lebrun, J.-C., Appourchaux, T., & Korzennik, S. G. 2004, *A&A*, 418, 295
- Martín, E. L., Delfosse, X., Basri, G., Goldman, B., Forveille, T., & Zapatero Osorio, M. R. 1999, *AJ*, 118, 2466
- McCarthy, C., & Zuckerman, B. 2004, *AJ*, 127, 2871
- Metchev, S. A., & Hillenbrand, L. A. 2006, *ApJ*, 651, 1166
- Monet, D. G., Dahn, C. C., Vrba, F. J., Harris, H. C., Pier, J. R., Luginbuhl, C. B., & Ables, H. D. 1992, *AJ*, 103, 638
- Monet, D. G., et al. 2003, *AJ*, 125, 984
- Oppenheimer, B. R., Golimowski, D. A., Kulkarni, S. R., Matthews, K., Nakajima, T., Creech-Eakman, M., & Durrance, S. T. 2001, *AJ*, 121, 2189
- Perryman, M. A. C., Brown, A. G. A., Lebreton, Y., Gomez, A., Turon, C., de Strobel, G. C., Mermilliod, J. C., Robichon, N., Kovalevsky, J., & Crifo, F. 1998, *A&A*, 331, 81
- Perryman, M. A. C., et al. 1997, *A&A*, 323, L49
- Pinfield, D. J., Jones, H. R. A., Lucas, P. W., Kendall, T. R., Folkes, S. L., Day-Jones, A. C., Chappelle, R. J., & Steele, I. A. 2006, *MNRAS*, 368, 1281
- Potter, D., Martín, E. L., Cushing, M. C., Baudoz, P., Brandner, W., Guyon, O., & Neuhäuser, R. 2002, *ApJ*, 567, L133
- Potter, D. E., Martín, E. L., & Cushing, M. C. 2003, in *IAU Symposium*, Vol. 211, *Brown Dwarfs*, ed. E. Martín, 265

- Pravdo, S. H., Shaklan, S. B., Wiktorowicz, S. J., Kulkarni, S., Lloyd, J. P., Martinache, F., Tuthill, P. G., & Ireland, M. J. 2006, *ApJ*, 649, 389
- Preibisch, T., & Feigelson, E. D. 2005, *ApJS*, 160, 390
- Press, W. H., Teukolsky, S. A., Vetterling, W. T., & Flannery, B. P. 1992, *Numerical Recipes in C: The Art of Scientific Computing* (Cambridge: Cambridge University Press, 2nd ed.)
- Rayner, J. T., Toomey, D. W., Onaka, P. M., Denault, A. J., Stahlberger, W. E., Watanabe, D. Y., & Wang, S. 1998, in *Proc. SPIE: Infrared Astronomical Instrumentation*, ed. A. M. Fowler, Vol. 3354, 468–479
- Reid, I. N., Burgasser, A. J., Cruz, K. L., Kirkpatrick, J. D., & Gizis, J. E. 2001, *AJ*, 121, 1710
- Sarajedini, A., von Hippel, T., Kozhurina-Platais, V., & Demarque, P. 1999, *AJ*, 118, 2894
- Schaefer, G. H., Simon, M., Nelan, E., & Holfeltz, S. T. 2003, *AJ*, 126, 1971
- Simon, M., Bender, C., & Prato, L. 2006, *ApJ*, 644, 1183
- Simons, D. A., & Tokunaga, A. 2002, *PASP*, 114, 169
- Skumanich, A. 1972, *ApJ*, 171, 565
- Soderblom, D. R., Fedele, S. B., Jones, B. F., Stauffer, J. R., & Prosser, C. F. 1993a, *AJ*, 106, 1080
- Soderblom, D. R., Jones, B. F., Balachandran, S., Stauffer, J. R., Duncan, D. K., Fedele, S. B., & Hudon, J. D. 1993b, *AJ*, 106, 1059
- Soderblom, D. R., Pilachowski, C. A., Fedele, S. B., & Jones, B. F. 1993c, *AJ*, 105, 2299
- Stassun, K. G., Mathieu, R. D., & Valenti, J. A. 2006, *Nature*, 440, 311
- Stelzer, B., & Neuhäuser, R. 2001, *A&A*, 377, 538
- Stephens, D. C., & Leggett, S. K. 2004, *PASP*, 116, 9
- Stern, R. A., Schmitt, J. H. M. M., & Kahabka, P. T. 1995, *ApJ*, 448, 683
- Stone, R. C. 1984, *A&A*, 138, 275
- Takeda, G., Ford, E. B., Sills, A., Rasio, F. A., Fischer, D. A., & Valenti, J. A. 2007, *ApJS*, 168, 297
- Tegmark, M., et al. 2004, *Phys. Rev. D*, 69, 103501
- Tokunaga, A. T., Simons, D. A., & Vacca, W. D. 2002, *PASP*, 114, 180
- Vacca, W. D., Cushing, M. C., & Rayner, J. T. 2003, *PASP*, 115, 389

- Valenti, J. A., & Fischer, D. A. 2005, *ApJS*, 159, 141
- van Leeuwen, F. 2007, *Hipparcos, the New Reduction of the Raw Data (Hipparcos, the New Reduction of the Raw Data. By Floor van Leeuwen, Institute of Astronomy, Cambridge University, Cambridge, UK Series: Astrophysics and Space Science Library, Vol. 350 20 Springer Dordrecht)*
- VandenBerg, D. A., & Stetson, P. B. 2004, *PASP*, 116, 997
- Voges, W., et al. 1999, *A&A*, 349, 389
- Vrba, F. J., et al. 2004, *AJ*, 127, 2948
- Walter, F. M., & Berry, D. C. 1991, in *The Sun in Time*, ed. C. P. Sonett, M. S. Giampapa, & M. S. Matthews (Tucson: University of Arizona Press), 653
- Wilson, J. C., Kirkpatrick, J. D., Gizis, J. E., Skrutskie, M. F., Monet, D. G., & Houck, J. R. 2001, *AJ*, 122, 1989
- Wizinowich, P. L., Chin, J., Johansson, E., Kellner, S., Lafon, R., Le Mignant, D., Neyman, C., Stomski, P., Summers, D., Sumner, R., & van Dam, M. 2006, in *Presented at the Society of Photo-Optical Instrumentation Engineers (SPIE) Conference, Vol. 6272, Advances in Adaptive Optics II*. Edited by Ellerbroek, Brent L.; Bonaccini Calia, Domenico. *Proceedings of the SPIE, Volume 6272*, pp. 627209 (2006).
- Wright, J. T., Marcy, G. W., Butler, R. P., & Vogt, S. S. 2004, *ApJS*, 152, 261
- Zapatero Osorio, M. R., Lane, B. F., Pavlenko, Y., Martín, E. L., Britton, M., & Kulkarni, S. R. 2004, *ApJ*, 615, 958
- Zuckerman, B., Bessell, M. S., Song, I., & Kim, S. 2006, *ApJ*, 649, L115
- Zuckerman, B., & Song, I. 2004, *ARA&A*, 42, 685

A. Monte Carlo Simulations of HD 130948BC in *HST*/ACS Coronagraph Images

In order to robustly determine the systematic and random uncertainties in our PSF-fitting measurements of HD 130948BC in the 2002 and 2005 *HST*/ACS coronagraph data, we fit an array of simulated binary images constructed from images of single stars. No suitable single stars were present in any archival coronagraph images taken in the same filters as HD 130948BC (*F850LP* and *FR914M*). Therefore, we turned to the much richer archive of *F814W* coronagraph data, in

which we found numerous suitable single stars. We selected three of the highest S/N stars in the archive, all of which come from a 2003 March 25 UT observation of HD 163296 (GTO/ACS-9295, PI Ford). These two ≈ 2000 sec exposures were taken at two different roll angles, providing optimal subtraction of the background light due to the bright occulted star, and we used the second image (14:15 UT) to subtract the background from the first (11:07 UT). The locations of the three stars we selected sample very different subpixel locations, which is a potential source of systematic error for the fitting of the slightly undersampled ACS PSF. In the end, we found that no matter which single star we used, the resulting astrometry did not change significantly, so all results we quote from our Monte Carlo simulations refer to the highest S/N star. This star was scaled down by 3.3–5.7 mag to match the S/N of the science data, depending on the epoch and bandpass.

We created simulated binary images at the integer pixel separations that most closely approximated HD 130948BC at each epoch and telescope roll angle. Subpixel-shifted binary images are impossible to accurately create from one image of a single star because the ACS-HRC PSF is slightly undersampled, inhibiting accurate interpolation to a fraction of a pixel. For the 2002 epoch, we used an equal number of simulated binaries with integer separations of $(\Delta x, \Delta y) = (-3, 3)$ and $(\Delta x, \Delta y) = (-2, 3)$ to approximate HD 130948BC which had a measured separation of $(\Delta x, \Delta y) \approx (-2.5, 3.0)$. For the 2005 epoch, we used simulated binaries at integer pixel separations of $(\Delta x, \Delta y) = (-2, 1)$ and $(\Delta x, \Delta y) = (-1, 2)$. Each corresponds to a different roll angle in the science data, for which the actual best-fit separations were $(\Delta x, \Delta y) \approx (-1.8, 1.2)$ and $(\Delta x, \Delta y) \approx (-1.4, 1.8)$.

We scaled down the simulated binary images to match the peak counts of the science data then added photon noise assuming a gain of $2.2 \text{ e}^-/\text{DN}$ (from the ATODGAIN header keyword). We used a flux ratio of 0.25 mag, consistent with the flux ratio measured in the 2005 $F850LP$ data, when creating all simulated binary images. Since HD 130948BC itself is always located in the exact part of the residual background in which we would like to inject our simulated binaries in any given image, we instead injected them at a location 180° -symmetric to the location of HD 130948BC. This is motivated by the fact that the background light is visibly 180° -symmetric even on scales as small as a few pixels. (Note that this symmetry is not so perfect that rotated self-subtraction is preferred over roll subtraction for the removal of background light to the bright occulted star.) To account for some uncertainty in the exact 180° -symmetric point, we injected the simulated binary images at each location in a 3×3 pixel box centered on our best guess of the 180° -symmetric location. This also served to sample different realizations of the noise being added to the simulated binary images. We found that using a larger box size (e.g., 5×5) did not significantly change the results.

We then applied our PSF-fitting routine in an identical manner to the simulated binary images as to the science data, with one exception. Because the single star used to generate the simulated binary images is actually taken from an $F814W$ image, we used the appropriate $F814W$ TinyTim models in the simulations. By comparing the input separations, position angles (PAs, measured in degrees east from north), and flux ratios of the simulated binaries to the fitted values, we determined

the random error and any significant systematic offsets inherent in PSF-fitting routine.

We also investigated the effects of telescope defocus (e.g., due to breathing) and jitter on our PSF-fitting. In our analysis of *HST*/WFPC2 images of 2MASS J1534–2952AB (Liu et al. 2008), we found that allowing these as free parameters in the PSF significantly improved the residuals, producing slightly improved astrometric precision. For the 2002 observations of HD 130948BC, the best-fit defocus and jitter of the science data reached unrealistic values ($> 20 \mu\text{m}$; $> 20 \text{mas}$) when allowed as a free parameter, thus we fixed telescope defocus and jitter to zero for both the science data and the simulations of the 2002 epoch. For the 2005 epoch, we found a degeneracy between telescope defocus and the measured binary separation, in the sense that tighter binaries could be equally well fit if the amplitude of the defocus was allowed to be rather large ($+12 \mu\text{m}$). This may be intuitively understood since defocus essentially increases the extent of the PSF, so for a given binary footprint in a science image tighter separations can only be fit by increasing the defocus. The effect on the astrometry is indeed small (0.05–0.08 pix, 1–2 mas) but significant. Through the use of our Monte Carlo simulations, in which we know the true separation of our simulated binary images, we were able to break the degeneracy: allowing defocus as a free parameter artificially decreased the measured separation. Only values of the defocus larger than are typically observed ($\pm 10 \mu\text{m}$) produced this degeneracy. Therefore we fixed defocus and jitter to zero for both the science images and simulations of the 2005 epoch.

First, we consider the results for the 2002 epoch, where the science data come from four different bandpasses: *F850LP*, *FR914M* (8626 Å), *FR914M* (9402 Å), and *FR914M* (10248 Å). The separation of HD 130948BC at this epoch is $\sim 2\times$ larger than at the 2005 epoch, but the S/N is lower (see Figure 1), so it is not clear that the astrometric precision should be better. We found that the scatter among measurements taken in different bandpasses was consistent with the random error predicted by the simulations. In Table 1, we quote the individual measurements taken in different bandpasses with their respective offsets applied and with uncertainties given from the Monte Carlo simulations. The systematic offsets were small compared to the uncertainties (0.1–1.2 σ). To understand how to combine these measurements, we investigated the nature of the uncertainties through simulations where the S/N was varied over the equivalent of 0.0–7.5 mag of noise degradation. Since the S/N of the single star used to generate the simulated binaries is very high, this allows us to see what the error would be if the S/N were much higher or lower than the science data. If the astrometric uncertainties were truly independent with respect to our PSF-fitting routine, they should improve linearly with S/N (King 1983). We found that at low S/N the error in the 2002 epoch astrometry improved slightly less than linearly, which implies a significant systematic component to the error that cannot be reduced by averaging over multiple measurements. At high S/N , the error was constant over a wide range of S/N , implying a systematic noise floor. The S/N of the science data is near the boundary between these two error regimes, thus the uncertainty of the science data is dominated by the systematic component, and we cannot combine the individual measurements in different bandpasses assuming they are independent. Therefore, for the 2002 epoch, we use the single bandpass with the smallest error in both separation and PA, *FR914M*

(9402 Å), which is also the bandpass with the cleanest background subtraction, highest S/N , and lowest χ^2 from PSF-fitting.

Given the higher S/N of the 2005 data, our simulations show that our astrometric uncertainty is better than for the 2002 epoch, even though the binary is much tighter in the 2005 data. All of the systematic offsets predicted by our simulations were smaller than the predicted random errors. In Table 1, we quote the individual measurements after applying all systematic offsets and give the uncertainties determined from our simulations. To understand how to combine these measurements, we investigated the nature of the errors through simulations where the S/N was varied as described above for the 2002 epoch. We found that for all three 2005 measurements, the science data fall almost exactly between two regimes: (1) at high S/N the errors improve slightly less than linearly implying both random and systematic errors are significant; (2) at low S/N the errors improve linearly implying this regime is dominated by random noise. If our science data were in the noise-dominated regime, we could hope to reduce the errors by $\sqrt{3}$ by averaging the three measurements and adopting the standard error on the mean. However, since the data are in the high S/N regime, no further reduction of the uncertainty is possible due to a significant contribution from non-independent systematic errors. Therefore, we use the mean of the three 2005 *HST* measurements, with the typical (median) random error predicted by the Monte Carlo simulations as its uncertainty.

B. Monte Carlo Simulations of HD 130948BC in Keck NGS AO Images

For each epoch of Keck observations, we conducted simulations to determine the systematic and random errors inherent to our PSF-fitting routine. We created simulated binary images using the best available empirical Keck NGS AO PSF. The separation, PA, and flux ratio of each simulated binary were randomly drawn to be within 0.3 pixels, 3° , and 0.2 mag, respectively, of the measured values at that epoch. We used bilinear interpolation with cubic convolution to create a shifted but otherwise identical PSF image. The original and shifted PSFs were each scaled to match the typical peak fluxes of HD 130948BC at the given epoch. Because the empirical PSF image used to construct the simulated binary images was always of a higher S/N than the science data, random noise was added to the simulated binary images assuming Poisson statistics for the science data and infinite S/N for the empirical input PSF.

The empirical input PSFs for the 2007 January epoch simulations were images of the primary star HD 130948A taken in K_{cont} -band directly after obtaining K -band images of HD 130948BC. The Strehl ratio and FWHM of the images of HD 130948A were 0.10 ± 0.02 and 65.2 ± 4.1 mas, respectively. In February 2007, the next generation wavefront controller (NGWFC) was installed on Keck II (Wizinowich et al. 2006). Thus, for the remaining K_S - and K_{cont} -band epochs, we used the NGWFC bright star K -band PSFs ($R = 7.5, 12.6, 13.6$ mag) available on the Keck NGS AO

webpage⁹. We measured the Strehl ratio and FWHM of this set of three PSFs to be 0.51 ± 0.02 and 46.8 ± 0.9 mas. There is not a stark drop in Strehl or FWHM with NGS brightness because the Keck NGS AO system delivers similar on-axis image quality when the NGS is brighter than $R \approx 13$ mag. This PSF stability is also what enables our use of non-contemporaneous PSFs, which is further justified by the fact that the systematic offsets derived from these empirical PSFs improves the orbit fit (see §2.2). Finally, we used Keck NGS images of the bright star Gl 569A ($R = 9.4$ mag; Monet et al. 2003) taken in H_{cont} -band ($\lambda_c = 1.580 \mu\text{m}$, $\Delta\lambda = 0.023 \mu\text{m}$) on 2008 January 16 as the empirical input PSF for the 2007 July epoch simulations. The Strehl ratio and FWHM of these H -band PSFs were 0.29 ± 0.04 and 37.9 ± 0.6 mas, respectively. In summary, while the FWHM of the single PSFs we use in our simulations are comparable to the FWHM of the science images, the Strehl ratios are consistently somewhat worse than the science data (Table 2). Therefore, we expect that the uncertainties from our Monte Carlo simulations of the Keck astrometry may be slightly overestimated (this is consistent with our best fit orbit, which has reduced $\chi^2 < 1$).

Background light due to the primary star HD 130948A was added to the simulated binary images in order to accurately replicate our science images. To accomplish this, we utilized the 60° -symmetric nature of the hexagonal Keck PSF. We extracted subregions from each dithered image at 60° -symmetric locations relative to the location of HD 130948A. Though the central pixels of HD 130948A are saturated in these images, its location can be deduced (typically to better than ≈ 1 pixel) from the intersection of the 6 diffraction spikes. The extracted subregions were appropriately rotated to match the background at the location of HD 130948BC. This yielded a number of independent images of the background up to five times the number of dithered images at a given epoch. Some of the symmetric locations fell off the array, but there was always at least one symmetric location available for each dithered image. For each epoch, 10^3 simulated science images were constructed by random pairing of the extracted background images with the simulated binary images described above.

The hexagonal Keck Airy pattern is clearly visible in all science images, so care was taken to appropriately rotate the empirical input PSFs to match the rotation in the science images. This is important because the overlap of the first hexagonal Airy ring of one component with the core of the other is likely one of the major sources of systematic error in our PSF-fitting technique. The image rotator of the Keck AO system changes to keep the PA of the sky fixed with respect to NIRC2 during a set of observations. Thus, the telescope optics and resulting Airy pattern rotate with respect to NIRC2, and these angles were measured directly from the header of each science image. For instance, the 2007 March 25 observations were conducted over ≈ 8 minutes near transit, when the rotator is changing fastest, so the PSF rotated by $\approx 7^\circ$ with respect to the sky during that time.

⁹<http://www2.keck.hawaii.edu/optics/ngsao/>

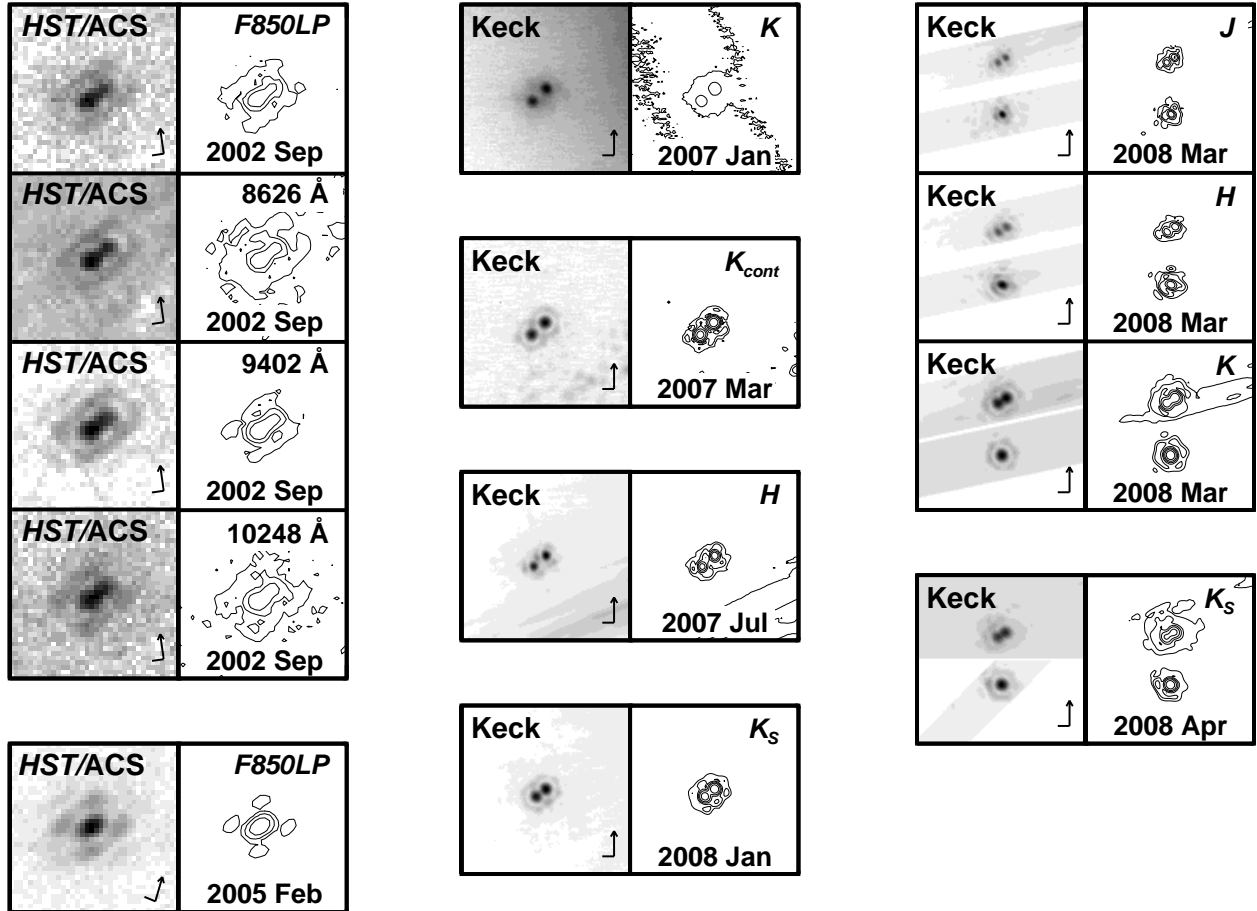


Fig. 1.— *HST* and Keck images of HD 130948BC at all epochs and bandpasses, shown chronologically by column. Unsaturated images of HD 130948A are shown alongside the HD 130948BC images for the last two epochs. For the most recent Keck epochs, interlaced short-exposure images of HD 130948A are also shown. For *HST* images, the background light due to the occulted primary has been optimally subtracted as described in the text. *HST* images are in either *F850LP* or the *FR914M* ramp filter, which produces nearly-monochromatic images, and we have labeled the images with the wavelength (LRFWAVE header keyword). We do not rotate the *HST* data so that north is up in order to preserve the somewhat undersampled nature of the data. Note that severe geometric distortion makes the cardinal directions in ACS-HRC images non-orthogonal. In the Keck images, light from the PSF halo and/or the diffraction spikes of the primary are typically visible. With the exception of the 2007 Jan epoch, during which seeing conditions were poor, the hexagonal Airy ring of the Keck PSF is visible in all the images. Both *HST* and Keck images are shown on the same scale, $1''.0$ on a side, with a square-root stretch for the grayscale images. Contours are drawn at 0.50, 0.25, 0.13, 0.06, and 0.03 of the peak pixel. For lower S/N images (i.e., all *HST* images and the 2007 Jan image) the two lowest contours are not drawn.

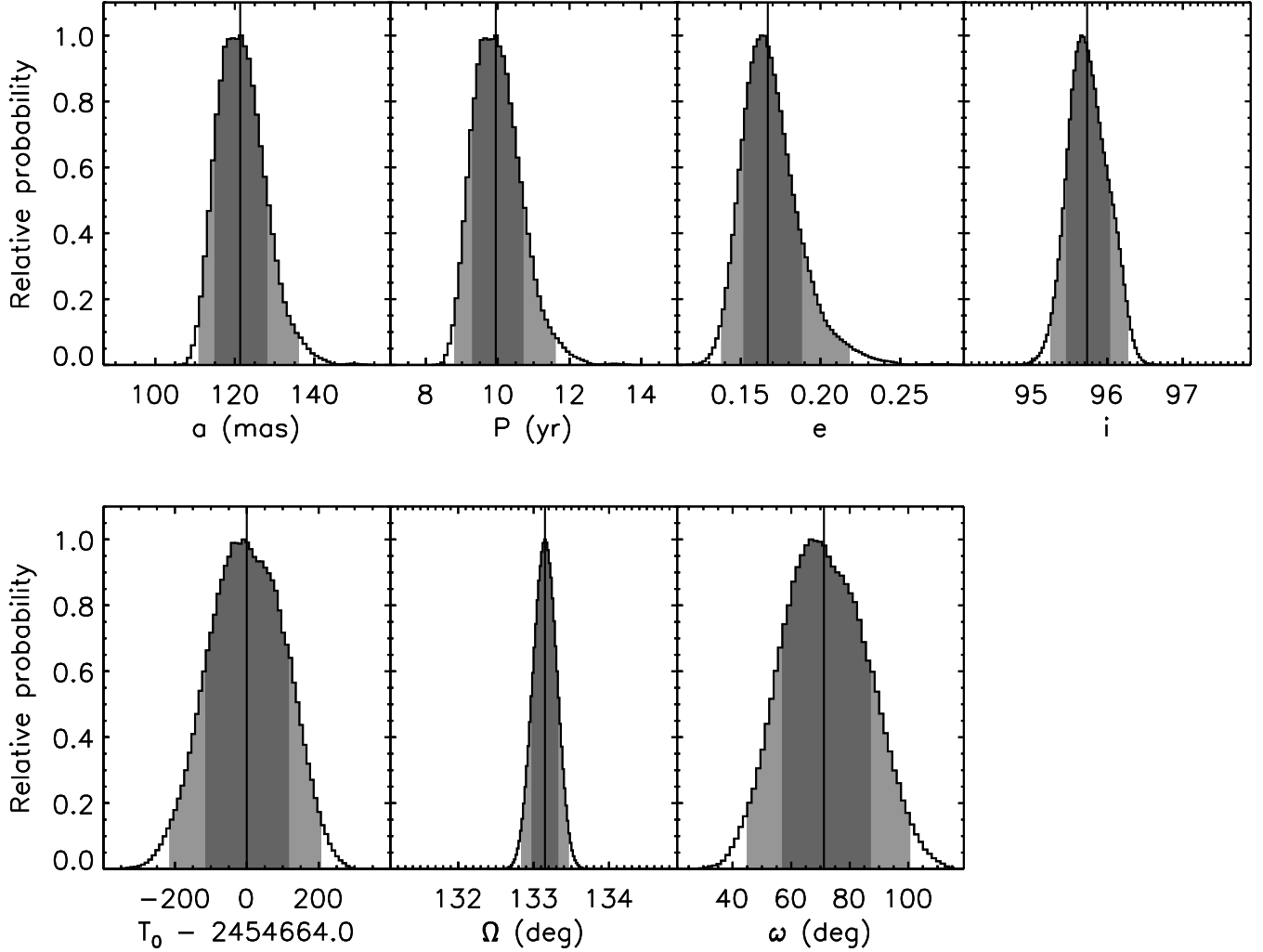


Fig. 2.— Probability distributions of all orbital parameters derived from the MCMC analysis: semimajor axis (a), orbital period (P), eccentricity (e), inclination (i), epoch of periastron (T_0), PA of the ascending node (Ω), and argument of periastron (ω). Each histogram is shaded to indicate the 68.3% and 95.5% confidence regions, which correspond to 1σ and 2σ for a normal distribution, and the solid vertical lines represent the median values. Note that T_0 is shown in days since 2008 Jul 16 12:00 UT for clarity.

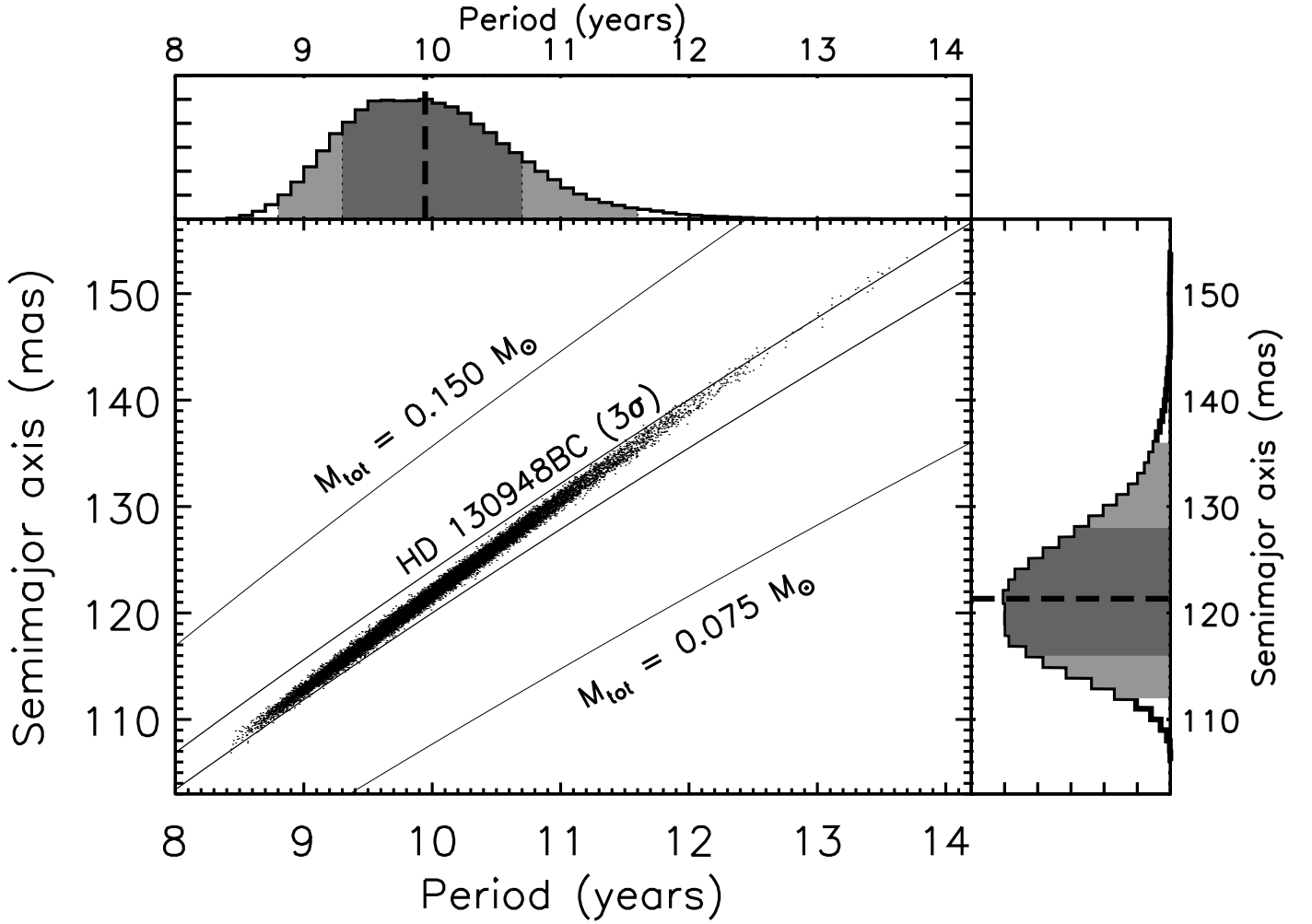


Fig. 3.— Results from the MCMC determination of the orbital period and semimajor axis for HD 130948BC. The central plot shows all the values in the MCMC chain. The locus illustrates the degeneracy between determining the orbital period and semimajor axis. Lines of constant mass are drawn in the central plot to show that the resulting mass precision is much better than simply adding the uncertainties in P and a in quadrature. The top and side plots show the resulting probability distributions of P and a . Each histogram is shaded to indicate the 68.3% and 95.5% confidence limits, which correspond to 1σ and 2σ for a normal distribution, and the dashed vertical lines represent the median values.

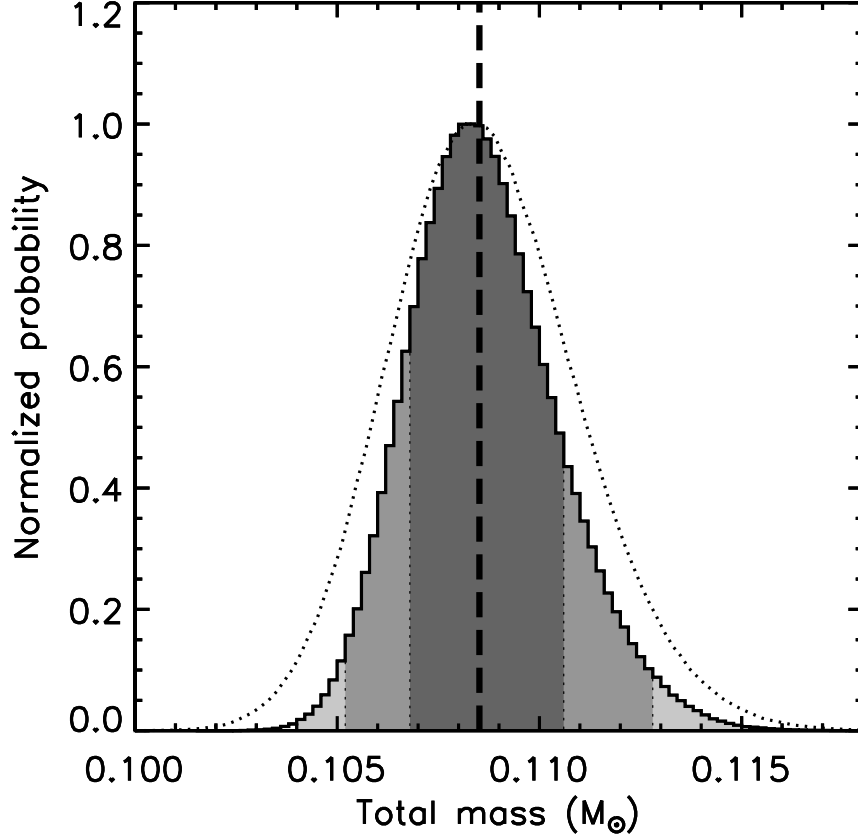


Fig. 4.— Probability distribution of the total mass of HD 130948BC resulting from our MCMC analysis. The histogram is shaded to indicate the 68.3%, 95.5%, and 99.7% confidence regions, which correspond to 1σ , 2σ , and 3σ for a normal distribution. The dashed line represents the median value of $0.1085 M_{\odot}$. The standard deviation of the distribution is $0.0018 M_{\odot}$. The dotted unshaded curve shows the final mass distribution after accounting for the additional 1.3% error due to the uncertainty in the *Hipparcos* parallax of HD 130948A; the result is essentially Gaussian. The confidence limits for both distributions are given in Table 4.

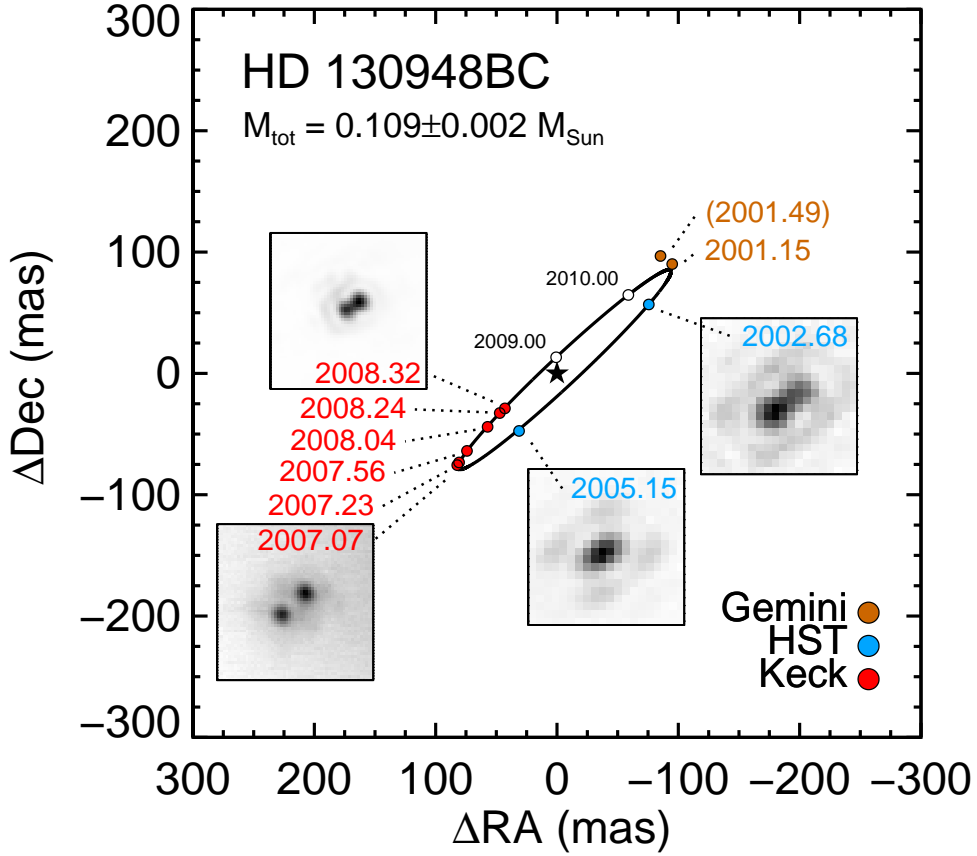


Fig. 5.— Keck (red), *HST* (blue), and Gemini (gold) relative astrometry for HD 130948BC along with the best-fit orbit using only the *HST* and Keck data. The empty circles are the predicted location of HD 130948C for this object in 2009 and 2010. The Gemini point from 2001.15 was extracted from Potter et al. (2003) and seems to follow the best-fit orbit well. The Gemini point measured directly from archival data (and consistent with the published values in Potter et al. 2002) is labeled in parentheses and is clearly discrepant from the best-fit orbit.

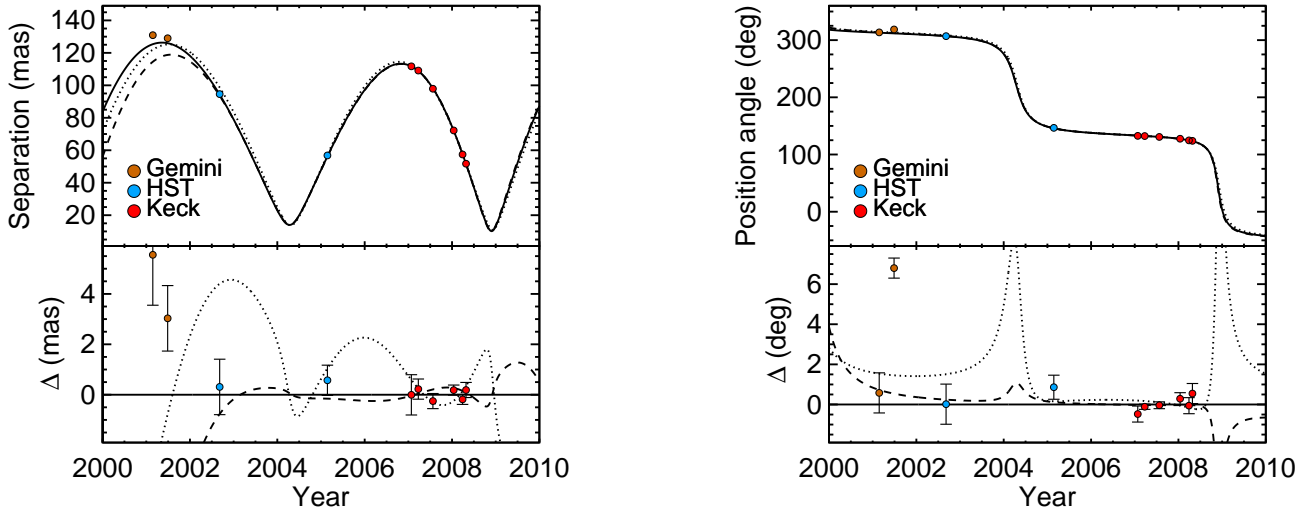


Fig. 6.— Keck (red), *HST* (blue), and Gemini (gold) measurements of the separation (*left*) and PA (*right*) of HD 130948BC. The best-fit orbit is shown: as a solid line for *HST* and Keck data only (our default solution); as a dashed line for *HST* and Keck data with the “extracted” Gemini data (2001.15 epoch); and as a dotted line for *HST* and Keck data with the “measured” Gemini data (2001.49 epoch). The bottom panels show the observed minus predicted separation and PA with observational error bars. This highlights the extreme discrepancy in the measured/published Gemini point in PA, even for the orbit in which it was included as a constraint (dotted). This shows that no physically plausible orbit can fit both the *HST*+Keck data and the measured/published Gemini point, indicating a systematic error in the PA of the Gemini point. There is a smaller discrepancy between the best-fit orbit and our “extracted” Gemini separation, possibly due to a systematic error in the instrument platescale in Wollaston-prism mode; however, the significance of the discrepancy is difficult to quantify because we cannot accurately assess the astrometric errors of the extracted data (we estimate 2 mas for the error in separation).

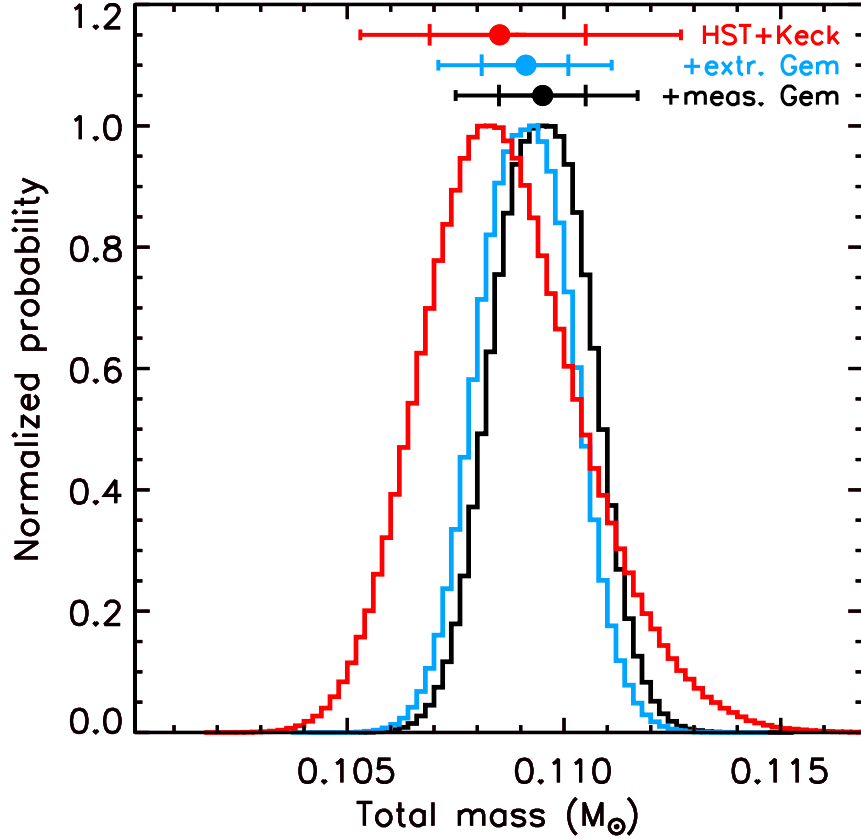


Fig. 7.— Total mass distribution from the MCMC analysis by fitting three different sets of astrometry: *HST* and Keck data only (our default solution, *red*); *HST* and Keck data with the “extracted” Gemini data (*gray*); *HST* and Keck data with the “measured” Gemini data (*black*). The filled circles indicate the median of the distributions, and the large (small) error bars indicate the 68.3% (95.5%) confidence limits, which correspond to 1σ (2σ) for a normal distribution. Adding the “extracted” Gemini astrometry to the *HST* and Keck data yields essentially the same dynamical mass but with a higher precision since it extends the time baseline of the observations. Adding the “measured” Gemini astrometry also improves the nominal precision, but introduces a more significant systematic offset. See § 2.3 for a discussion of the inconsistencies between the two Gemini measurements that cause this offset.

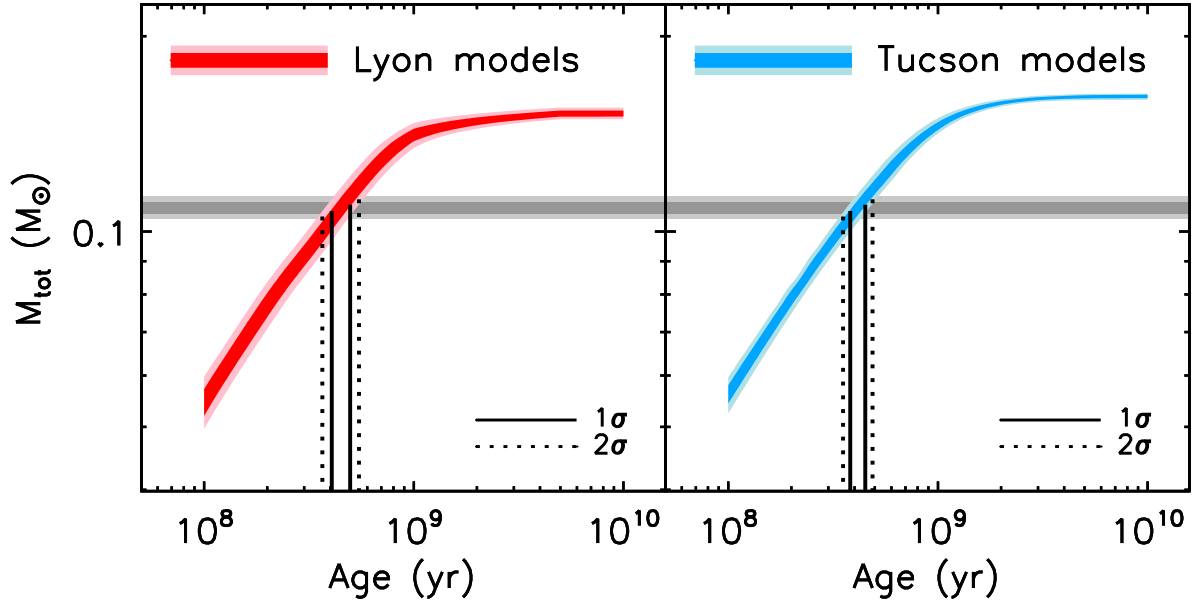


Fig. 8.— Total mass of HD 130948BC as a function of the age of the system that is predicted by evolutionary models, given the observed luminosities of the two components. By applying the measured total mass (M_{tot}), we inferred the age of HD 130948BC from evolutionary models (see §5.3). The colored shaded regions indicate the 1σ and 2σ ranges in M_{tot} corresponding to the luminosity uncertainties. At older ages, model substellar objects must be more massive in order to match the imposed luminosity constraint. At the oldest ages, the measured luminosities of HD 130948BC would correspond to a star at the bottom of the main-sequence, which causes the flattening of the M_{tot} -age curves. The horizontal gray bars show our 1σ and 2σ constraints on the total mass. The intersection of the measured M_{tot} with the model-predicted M_{tot} is shown by the solid (dotted) lines and corresponds to our 1σ (2σ) derived age range. Note that the model tracks shown here correspond only to objects with the same individual luminosities as HD 130948B and C and are not generally applicable to other binaries.

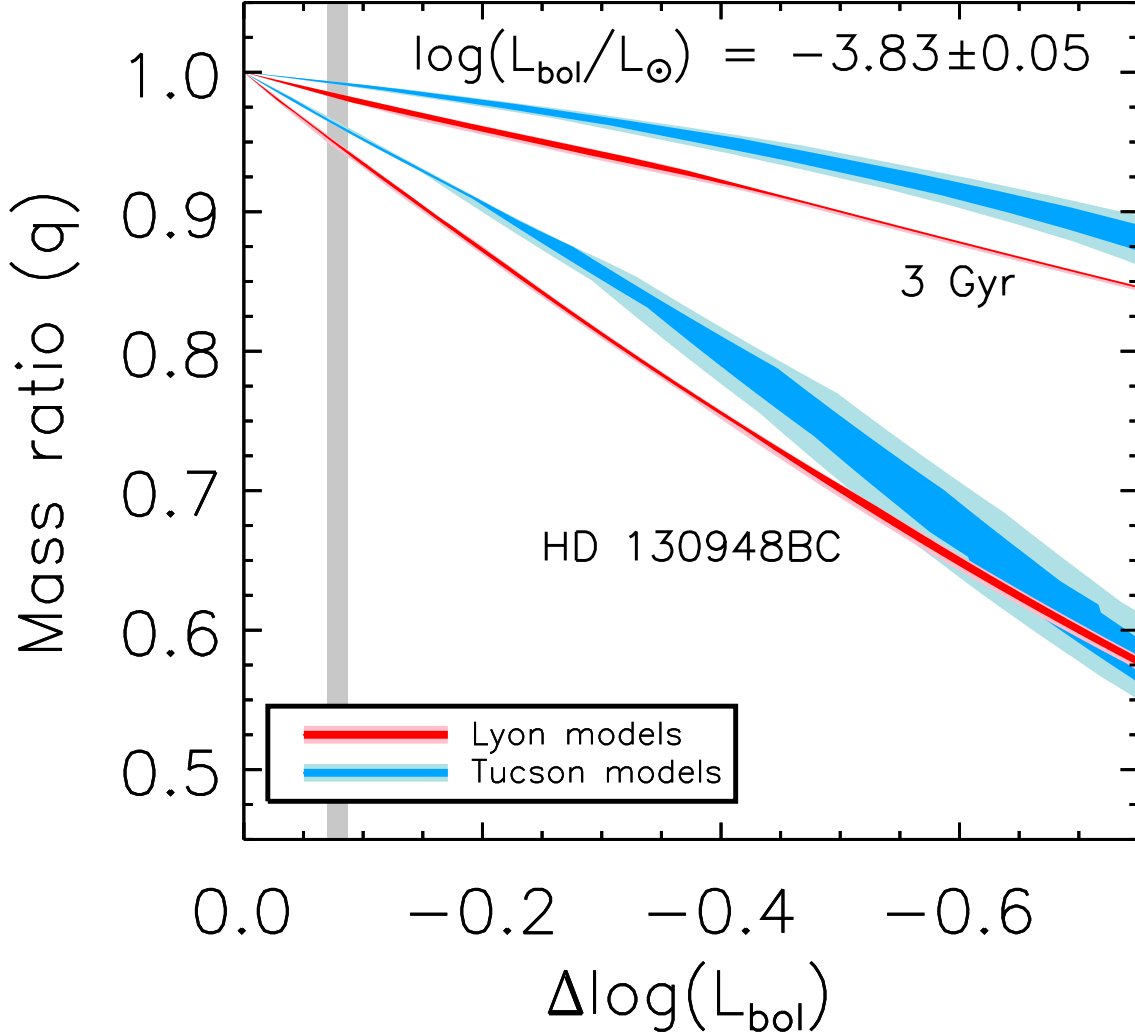


Fig. 9.— The model-predicted mass ratio for HD 130948BC as a function of the observed luminosity ratio. The colored regions are the 1σ and 2σ ranges of possible mass ratios that correspond to the 1σ and 2σ uncertainties in the luminosity of HD 130948B at the model-inferred age. The thin gray box shows the 1σ range of the measured luminosity ratio of HD 130948BC. A second set of colored regions shows the model-inferred mass ratios for an age of 3 Gyr, which illustrates the weak dependence of the assumed age on the mass ratio at near-unity flux ratios. Since the inferred mass ratio of a nearly equal-magnitude binary such as HD 130948BC is very insensitive both to the age of the system and to the evolutionary models used, the individual masses of HD 130948BC can be determined robustly. Note that these curves are not generally applicable to other binaries, since they are drawn for a small range in primary component L_{bol} and system age.

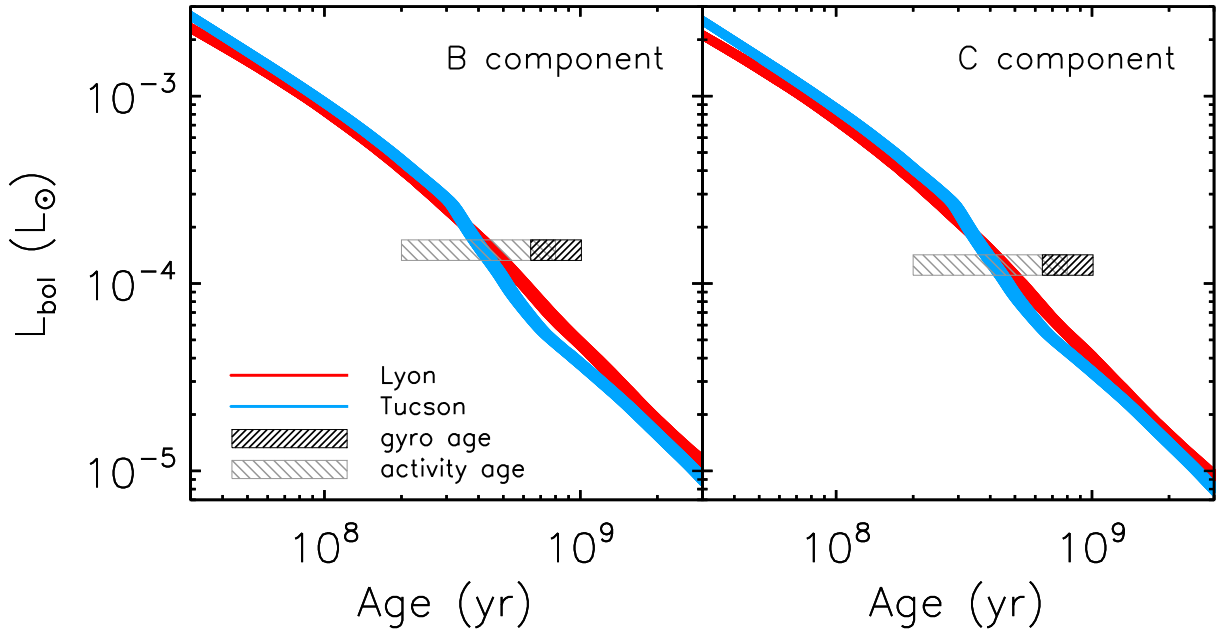


Fig. 10.— Isomass lines for evolutionary models with the individual masses of HD 130948BC. The colored line thicknesses encompass the 1σ errors in the individual masses. The hatched boxes indicate the constraints from the measured luminosities of HD 130948B and C and the age of HD 130948A using gyrochronology and chromospheric activity. The gyro age ($0.79^{+0.22}_{-0.15}$ Gyr) is inconsistent with the evolutionary models, implying that the models underpredict the luminosities of HD 130948BC by a factor of $\approx 2-3\times$.

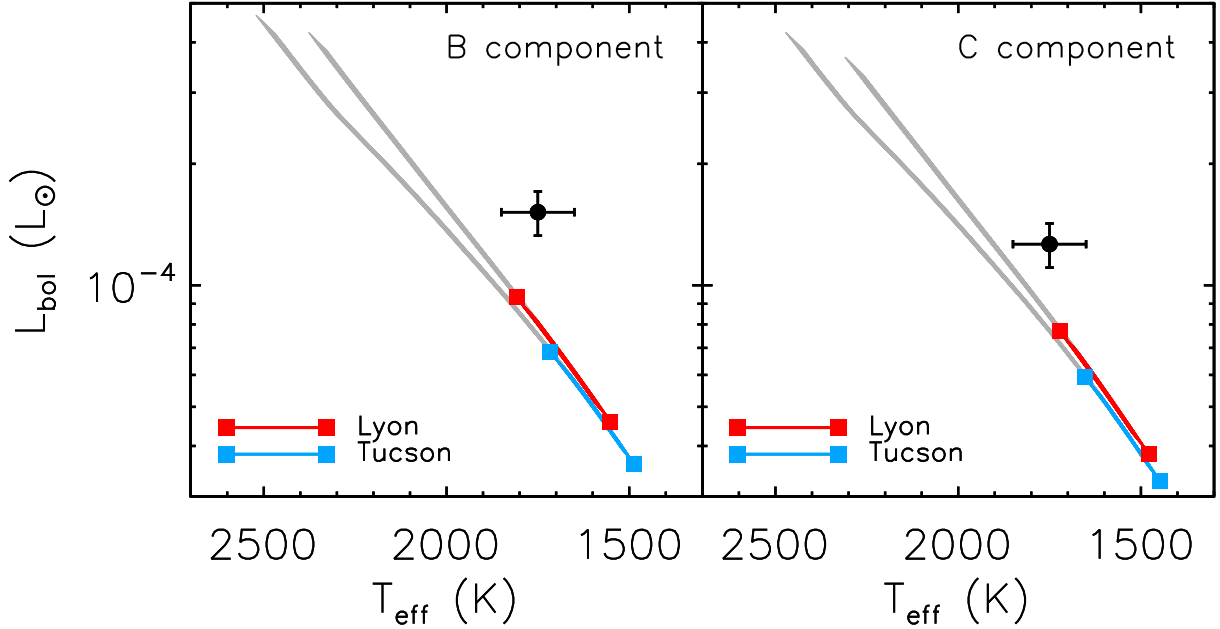


Fig. 11.— The Hertzsprung-Russell diagram showing isomass lines from evolutionary models corresponding to the individual masses of HD 130948BC. The plotted line thicknesses of these tracks encompass the 1σ errors in the individual masses. The red and blue colored regions correspond to the gyro age for HD 130948A ($0.79^{+0.22}_{-0.15}$ Gyr). The gray shaded regions correspond to the less precise chromospheric activity age (0.5 ± 0.3 Gyr). The Lyon and Tucson evolutionary models are nearly indistinguishable in their predicted T_{eff} and L_{bol} at these ages. The effective temperature determined for field L3–L5 dwarfs from spectral synthesis (1750 ± 100 K) is shown as a filled circle at the measured luminosities of HD 130948B and C. The numerous discrepancies between the models and the data seen here are discussed in §5.8.

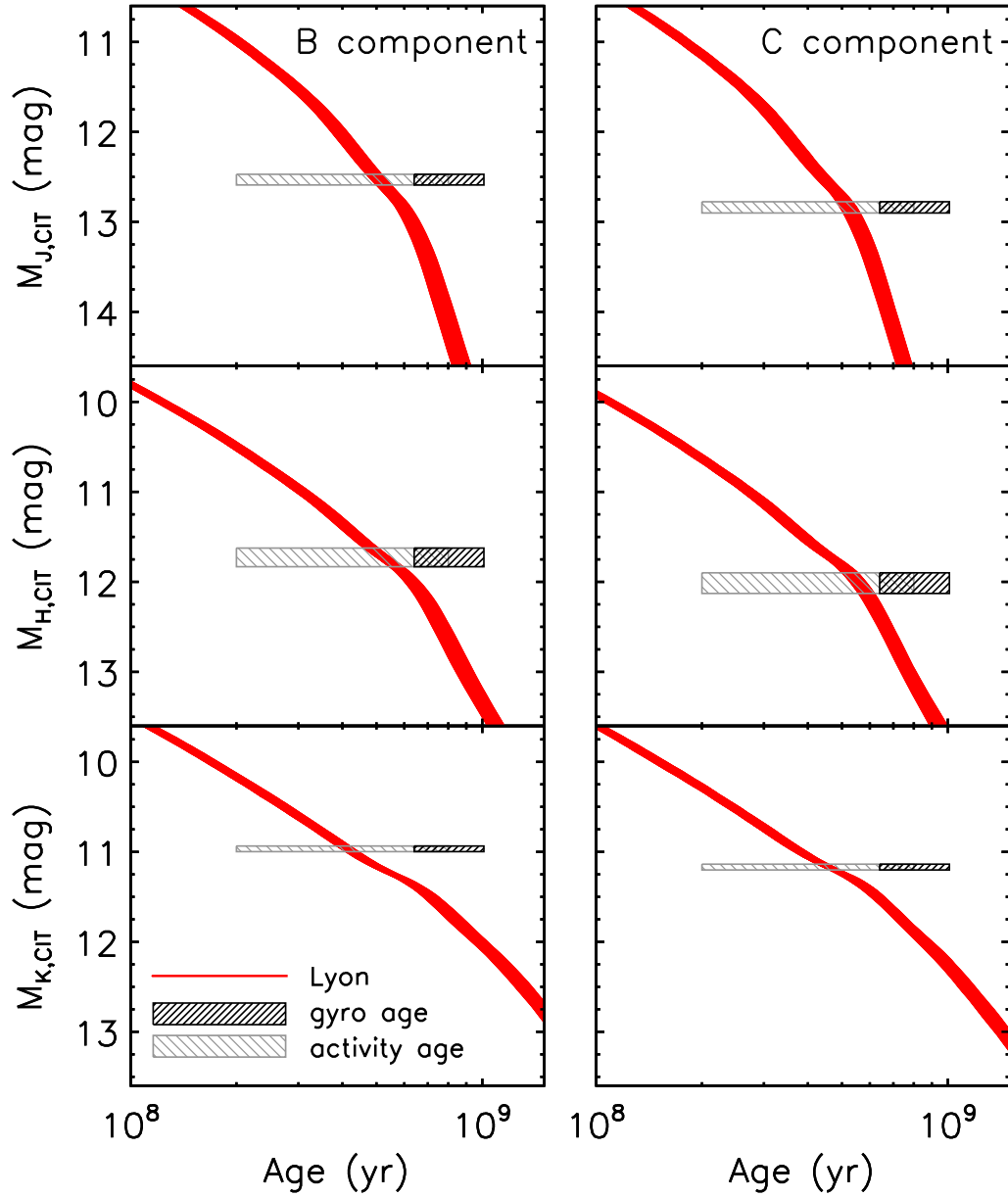


Fig. 12.— Isomass lines showing the evolution of J -, H -, and K -band absolute magnitudes for Lyon models with the individual masses of HD 130948BC. The colored line thicknesses encompass the 1σ errors in the individual masses. The hatched boxes indicate the constraints from the age of HD 130948A and the measured photometry of HD 130948B and C. The photometry shown here is on the CIT system, where we have converted our measured photometry of HD 130948BC from the MKO system using the relations of Stephens & Leggett (2004). The gyro age ($0.79^{+0.22}_{-0.15}$ Gyr) is inconsistent with the predicted fluxes, which is a reflection of the underpredicted bolometric luminosities of HD 130948BC (Figure 10). The model tracks intersect the measured photometry at different ages for different filters, which indicates inconsistencies in the model-predicted near-infrared colors (see Figure 13).

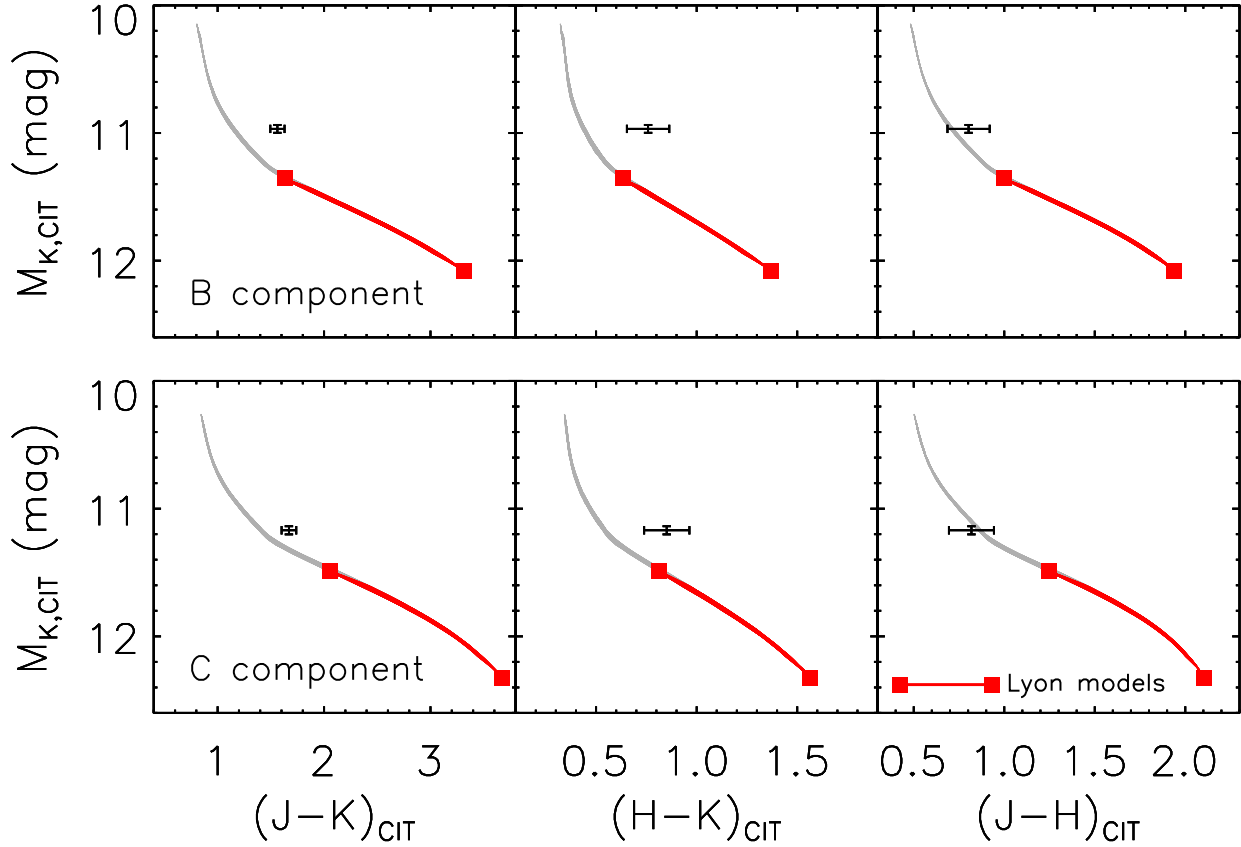


Fig. 13.— Color-magnitude diagrams showing the measured properties of HD 130948BC compared to Lyon evolutionary tracks for the masses of B and C. The plotted line thicknesses encompass the 1σ errors in the individual masses. The red colored regions correspond to the gyro age for HD 130948A ($0.79^{+0.22}_{-0.15}$ Gyr). The gray shaded regions correspond to the less precise activity age (0.5 ± 0.3 Gyr). In general, the measured colors are discrepant from that predicted by evolutionary models. Thus, evolutionary models will generally not yield accurate mass and/or age estimates for field L dwarfs from techniques using color-magnitude diagrams alone.

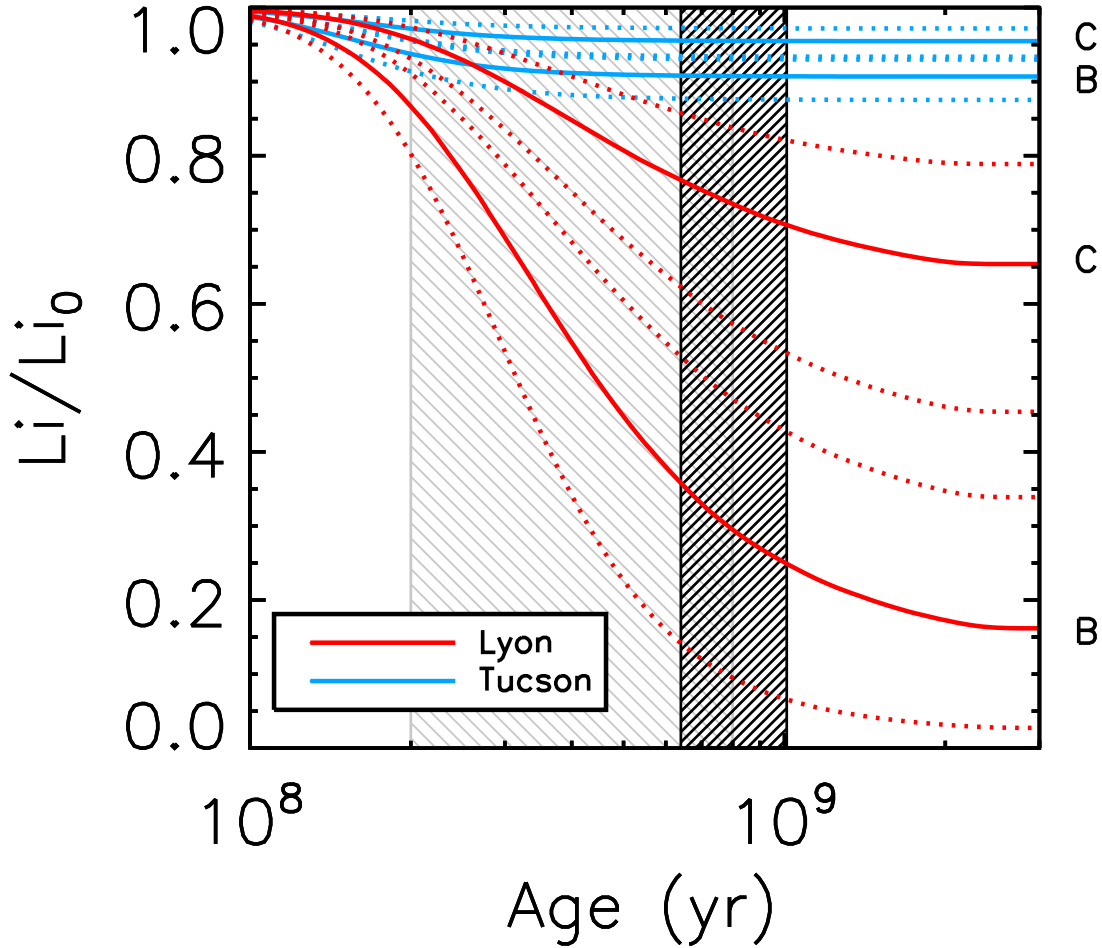


Fig. 14.— Lithium depletion as a function of age as predicted by evolutionary models. The solid lines correspond to the individual masses of the B and C components of HD 130948BC (C has a higher lithium fraction). These lines are bracketed by dotted lines that correspond to the 1σ uncertainties in the individual masses. The ordinate is the fraction of primordial lithium remaining. The hatched black (gray) box indicates the constraint from the age of HD 130948A estimated from gyrochronology (chromospheric activity). The Lyon models predict that all objects more massive than $\gtrsim 0.055 M_{\odot}$ eventually deplete most of their primordial lithium, while the Tucson models predict that this occurs only for objects more massive than $\gtrsim 0.062 M_{\odot}$. For the Lyon models, the components of HD 130948BC straddle the lithium-burning limit, while for the Tucson models neither component is expected to have depleted a significant amount of lithium. Thus, the age and individual masses of HD 130948BC are ideal for discriminating between these two sets of models with resolved optical spectroscopy designed to detect lithium absorption at 6708 Å. This would provide the only direct empirical constraint to date on the theoretical timescale and mass limit of lithium-burning in brown dwarfs, which are the basis for the “cluster lithium test” (e.g., Basri 1998) and the proposed “binary lithium test” (Liu & Leggett 2005).

Table 1. *HST*/ACS-HRC Coronagraph (1''8 Spot) Observations

Date/Start Time (UT)	t_{exp} (s)	ρ (mas)	PA ($^{\circ}$)	Δf (mag)	Filter	Note
2002 Sep 6/05:15	30	97.8 \pm 1.7	307.0 \pm 1.4	0.47 \pm 0.05	<i>F850LP</i>	1
2002 Sep 6/04:51	200	99.3 \pm 1.1	307.9 \pm 1.1	0.72 \pm 0.05	<i>FR914M</i> (8626 Å)	2
2002 Sep 6/04:56	200	94.6 \pm 1.1	306.9 \pm 1.0	0.41 \pm 0.04	<i>FR914M</i> (9402 Å)	3
2002 Sep 6/05:01	200	96.1 \pm 1.7	308.9 \pm 1.6	0.38 \pm 0.08	<i>FR914M</i> (10248 Å)	4
2002 Sep 6		94.6\pm1.1	306.9\pm1.0	...		
2005 Feb 23/15:39	300	56.8 \pm 0.6	144.9 \pm 0.5	0.19 \pm 0.03	<i>F850LP</i>	1
2005 Feb 23/17:15	300	56.4 \pm 0.9	146.4 \pm 0.6	0.24 \pm 0.06	<i>F850LP</i>	1
2005 Feb 23/18:46	300	57.3 \pm 0.6	148.6 \pm 0.6	0.30 \pm 0.05	<i>F850LP</i>	1
2005 Feb 23		56.8\pm0.6	146.6\pm0.6	0.24\pm0.05	<i>F850LP</i>	

Note. — Source of image used for background subtraction: (1)—HD 130948A, *F850LP*, 2005 Feb 23 UT; (2)— α Cen A, *FR914M* (8495 Å), 2004 Aug 7 UT; (3)— α Cen A, *FR914M* (9282 Å), 2004 Aug 7 UT; (4)— α Cen A, *FR914M* (10500 Å), 2003 Sep 12 UT.

Table 2. Keck NGS AO Observations

Date/Start Time (UT)	Filter ^a	$N \times t_{exp}$ (s) ^b	Airmass	FWHM (mas) ^c	Strehl ratio ^c	ρ (mas) ^d	P.A. ($^{\circ}$) ^d	Δf (mag)
2007 Jan 26/14:03	<i>K</i>	10×36	1.28	57.0±4.0	0.26±0.11	111.7±0.8	132.6 ±0.4	0.25 ±0.03
2007 Mar 25/12:41	<i>K_{cont}</i>	6×30	1.01	47.8±0.1	0.64±0.02	109.1±0.4	132.28±0.13	0.19 ±0.02
2007 Jul 25/05:41	<i>H</i>	9×30	1.01	35.7±0.6	0.42±0.09	97.9±0.3	130.73±0.17	0.19 ±0.05
2008 Jan 15/16:37	<i>K_S</i>	12×30	1.03	48.0±0.7	0.58±0.07	72.2±0.2	127.6 ±0.3	0.15 ±0.03
2008 Mar 29/13:38	<i>K</i>	14×30	1.03	49.1±0.3	0.65±0.02	57.4±0.2	124.7 ±0.4	0.197±0.003
2008 Mar 29/14:09	<i>J</i>	8×60	1.07	32.4±0.8	0.28±0.02	57.3±0.6	124.6 ±0.6	0.305±0.014
2008 Mar 29/15:46	<i>H</i>	6×30	1.36	41.8±1.1	0.35±0.03	58.4±0.6	124.1 ±0.7	0.29 ±0.02
2008 Apr 27/14:32	<i>K_S</i>	3×30	1.61	48.5±0.5	0.63±0.03	51.7±0.3	123.9 ±0.5	0.199±0.005

^aAll photometry on the MKO system.

^b N is the number of dithered images, each of exposure time t_{exp} , taken at that epoch.

^cComputed as described in the text using a $0''.75$ aperture, except for the 2007 Jan 26 epoch which required a smaller aperture ($0''.5$) because poor image quality led to increased flux contamination from HD 130948A. The quoted value and its error correspond to the mean and RMS of the set of dithered images.

^dThe tabulated errors are computed by adding in quadrature the uncertainty in the NIRC2 pixel scale and orientation and the uncertainty that is predicted for each epoch from the Monte Carlo simulations described in the text. We used a weighted average of the astrometric calibration from Pravdo et al. (2006), with a pixel scale of 9.963 ± 0.011 mas/pixel and an orientation for the detector's $+y$ -axis of -0.13 ± 0.07 east of north.

Table 3. Near-infrared MKO Photometry of HD 130948ABC

Property	HD 130948A	HD 130948B	HD 130948C	Reference
J (mag)	4.797 ± 0.022	13.81 ± 0.06	14.12 ± 0.06	1,2
H (mag)	4.515 ± 0.022	13.04 ± 0.10	13.33 ± 0.11	1,2
K (mag)	4.458 ± 0.020	12.26 ± 0.03	12.46 ± 0.03	1,2

References. — (1) This work; (2) Cutri et al. (2000).

Table 4. Derived Orbital Parameters for HD 130948BC

Parameter	MCMC			ORBIT [†]
	Median	68.3% c.l.	95.5% c.l.	
Semimajor axis a (mas)	121	−6, 6	−10, 14	121±7
Orbital period P (yr)	9.9	−0.6, 0.7	−1.1, 1.6	9.9±0.8
Eccentricity e	0.167	−0.015, 0.020	−0.03, 0.05	0.163±0.019
Inclination ^a i (°)	95.7	−0.2, 0.3	−0.5, 0.5	95.8±0.3
Time of periastron passage $T_0 - 2454664.0^b$ (JD)	0	−110, 110	−200, 200	14±130
PA of the ascending node Ω (°)	133.15	−0.16, 0.15	−0.3, 0.3	133.14±0.15
Argument of periastron ω (°)	71	−14, 15	−30, 30	73±18
Total mass (M_\odot): fitted ^c	0.1085	−0.0017, 0.0019	−0.003, 0.004	0.1083±0.0019
Total mass (M_\odot): final ^d	0.109	−0.002, 0.002	−0.004, 0.005	0.108±0.002
Reduced χ^2	1.14	1.14

[†]The orbital parameters determined by ORBIT are listed along with their linearized 1σ errors.

^aBy convention, $i > 90^\circ$ denotes that the sky PA is decreasing over time (clockwise motion), rather than increasing (counterclockwise).

^b2008 Jul 16 12:00:00.0 UT

^cThe “fitted” total mass represents the direct results from fitting the observed orbital motion of the two components. For the linearized ORBIT error, the covariance between P and a is taken into account.

^dThe “final” total mass includes the additional 1.3% error in the mass from the *Hipparcos* parallax of HD 130948A. This final mass distribution is essentially Gaussian.

Table 5. Age Estimates for HD 130948A

Age indicator	Age (Gyr)				Ref.
	Estimate	68.3% c.l.	95.5% c.l.	Precision (1σ)	
Stellar rotation (“gyrochronology”)	0.79	0.64–1.01	0.53–1.32	$\approx 25\%$	1
	0.65	0.55–0.78	0.47–0.93	$\approx 20\%$	2
Chromospheric activity (Ca II HK emission)	0.5	0.2–0.8	...	$\approx 60\%$	1
Stellar isochrones	0.72	...	0.32–2.48	$\approx 2\times$	3
X-ray activity [†]	...	0.1–0.6	1,4,5,6
Lithium depletion [†]	...	0.1–0.6	7

[†]These indicators do not give quantifiable age estimates or corresponding uncertainties. They do show that the age of HD 130948A is generally consistent with stars in the Hyades and Pleiades, thus we adopt these clusters’ ages as the 1σ range.

References. — (1) Mamajek & Hillenbrand (2008); (2) Barnes (2007); (3) Takeda et al. (2007); (4) Stern et al. (1995); (5) Gaidos (1998); (6) Stelzer & Neuhäuser (2001); (7) Soderblom et al. (1993a,b,c).

Table 6. Measured Properties of HD 130948BC

Property	HD 130948B	HD 130948C	Note
M_{tot} (M_{\odot})	0.109±0.002		1
d (pc)	18.18±0.08		2
Spectral Type	L4±1	L4±1	3
BC_K (mag)	3.33±0.13	3.34±0.13	1,4
ΔBC_K (mag)	0.00±0.02		1,4
$J - H$ (mag)	0.77±0.12	0.79±0.13	1
$H - K$ (mag)	0.78±0.10	0.87±0.11	1
$J - K$ (mag)	1.55±0.07	1.66±0.07	1
M_J (mag)	12.51±0.06	12.82±0.06	1
M_H (mag)	11.74±0.10	12.03±0.11	1
M_K (mag)	10.96±0.03	11.16±0.03	1
ΔK (mag)	0.197±0.008		1
$\log(L_{bol}/L_{\odot})$	-3.82±0.05	-3.90±0.05	1
$\Delta \log(L_{bol})$	0.079±0.008		1

References. — (1) This work; (2) van Leeuwen (2007); (3) Goto et al. (2002); (4) Golimowski et al. (2004).

Table 7. Evolutionary Model Inferred Properties of HD 130948BC

Property	Median	68.3% c.l.	95.5% c.l.
Tucson Models (Burrows et al. 1997)			
System			
Age (Gyr)	0.41	−0.03, 0.04	−0.06, 0.08
q (M_C/M_B)	0.962	−0.003, 0.003	−0.009, 0.009
ΔT_{eff} (K)	90	−8, 7	−22, 22
$\text{Li}_C/\text{Li}_B^\dagger$	1.049	−0.014, 0.011	−0.02, 0.03
Component B			
M_B (M_\odot)	0.0554	−0.0013, 0.0012	−0.002, 0.002
$T_{\text{eff},B}$ (K)	2040	−50, 50	−110, 110
$\log(g_B)$ (cgs)	5.196	−0.017, 0.017	−0.03, 0.03
R_B (R_\odot)	0.0983	−0.0011, 0.0011	−0.002, 0.002
Li_B/Li_0	0.91	−0.03, 0.03	−0.07, 0.05
Component C			
M_C (M_\odot)	0.0532	−0.0011, 0.0012	−0.002, 0.002
$T_{\text{eff},C}$ (K)	1950	−50, 50	−110, 110
$\log(g_C)$ (cgs)	5.179	−0.017, 0.017	−0.03, 0.03
R_C (R_\odot)	0.0983	−0.0010, 0.0010	−0.002, 0.002
Li_C/Li_0	0.96	−0.02, 0.02	−0.05, 0.03
Lyon Models (DUSTY; Chabrier et al. 2000)			
System			
Age (Gyr)	0.45	−0.04, 0.05	−0.08, 0.10
q (M_C/M_B)	0.948	−0.005, 0.005	−0.013, 0.012
ΔT_{eff} (K)	85	−7, 7	−21, 21
$\text{Li}_C/\text{Li}_B^\dagger$	1.6	−0.3, 1.0	−0.5, 3.5
Component B			
M_B (M_\odot)	0.0558	−0.0012, 0.0012	−0.002, 0.002
$T_{\text{eff},B}$ (K)	1990	−50, 50	−100, 90
$\log(g_B)$ (cgs)	5.143	−0.019, 0.019	−0.04, 0.04
R_B (R_\odot)	0.1048	−0.0016, 0.0017	−0.003, 0.004
Li_B/Li_0	0.50	−0.23, 0.18	−0.4, 0.3
Component C			
M_C (M_\odot)	0.0528	−0.0012, 0.0012	−0.002, 0.002
$T_{\text{eff},C}$ (K)	1900	−50, 50	−100, 90
$\log(g_C)$ (cgs)	5.122	−0.019, 0.019	−0.04, 0.04
R_C (R_\odot)	0.1045	−0.0015, 0.0016	−0.003, 0.003
Li_C/Li_0	0.83	−0.13, 0.08	−0.31, 0.12

† Ratio of the lithium abundance of the two components.